Molecular basis of Kar9-Bim1 complex function during mating and spindle positioning

Cristina Manatschal[a,†,‡], Ana-Maria Farcas[b,†], Miriam Steiner Degen[a,§], Mathias Bayer[b], Anil Kumar[a], Christiane Landgraf[c], Rudolf Volkmer[c], Yves Barral[b,*], and Michel O. Steinmetz[a,*]
[a]Laboratory of Biomolecular Research, Department of Biology and Chemistry, Paul Scherrer Institut, CH-5232 Villigen PSI, Switzerland; [b]Institute of Biochemistry, Biology Department, ETH Zürich, CH-8093 Zürich, Switzerland; [c]Institut für Medizinische Immunologie, Charité-Universitätsmedizin Berlin, 10117 Berlin, Germany

ABSTRACT The Kar9 pathway promotes nuclear fusion during mating and spindle alignment during metaphase in budding yeast. How Kar9 supports the different outcome of these two divergent processes is an open question. Here we show that three sites in the C-terminal disordered domain of Kar9 mediate tight Kar9 interaction with the C-terminal dimerization domain of Bim1 (EB1 orthologue). Site1 and Site2 contain SxIP motifs; however, Site3 defines a novel type of EB1-binding site. Whereas Site2 and Site3 mediate Kar9 recruitment to microtubule tips, nuclear movement, and karyogamy, only Site2 functions in spindle positioning during metaphase. Site1 in turn plays an inhibitory role during mating. Additionally, the Kar9-Bim1 complex is involved in microtubule-independent activities during mating. Together our data reveal how multiple and partially redundant EB1-binding sites provide a microtubule-associated protein with the means to modulate its biochemical properties to promote different molecular processes during cell proliferation and differentiation.

INTRODUCTION

The life cycle of budding yeast is articulated around a state of vegetative proliferation and a mode of sexual transitions and differentiation. In the proliferative state, yeast cells remain stable in one ploidy state (haploid or diploid). Here the mother cell duplicates and divides its cellular components to generate daughter cells (buds) similar to itself. Sexual mating and sporulation, on the other hand, imply changes in ploidy: mating drives haploid cells of opposite mating types to fuse and form diploid zygotes that can initiate diploid proliferation, while meiosis governs the generation of haploid cells that can resume proliferation (Herskowitz, 1988). Remarkably, a common requirement for both asexual and sexual stages of the yeast life cycle is the ability to appropriately position the nucleus of the cell. During division, the metaphase nucleus must localize to the predetermined division plane and align its spindle along the mother–bud axis. Only then can the cell equally distribute the sister chromatids to its daughters and maintain the genome throughout generations. During mating, the two partner cells of opposite mating types sense each other's presence through pheromone signaling and develop a cellular protrusion, called a shmoo, toward each other. Once the two shmoos meet and the two cells fuse, giving rise to a zygote (Hartwell, 1973), mating is completed through the fusion of the two parental nuclei into a diploid nucleus; this process is referred to as karyogamy. For this to be achieved, the two partner nuclei first need to migrate toward the converging shmoo tips during shmoo growth, a process called nuclear congression. Then the two spindle pole bodies (SPBs, the yeast equivalent of centrosomes), which are embedded in the nuclear envelope, must migrate toward each other upon cell fusion and trigger the fusion of the two nuclear envelopes with each other (Conde and Fink, 1976; Kurihara et al., 1994; Maddox et al., 1999).

Interestingly, the same molecular players drive nuclear positioning during vegetative proliferation and sexual differentiation: within metaphase cells, the Kar9 pathway, comprising the proteins Kar9 (karyogamy mutant 9), Bim1 (orthologue of EB1), and the type V myosin motor Myo2, governs nuclear positioning and spindle alignment with the mother–bud axis to facilitate the proper division of the mother nucleus into two daughter nuclei (Miller and Rose, 1998; Korinek et al., 2000). During mating, the same pathway ensures the movement and orientation of the partner nuclei toward the shmoo tip (Kurihara et al., 1994; Molk et al., 2006) and facilitates their subsequent fusion. How the Kar9 pathway functions in these divergent processes and whether proper functioning of these molecules requires that their biochemical properties are adapted to each situation are unknown.

Kar9 localizes to the SPB and plus ends of microtubules in a Bim1-dependent manner. Its localization during vegetative cycles is asymmetric, in the sense that the protein is restricted to only one of the two SPBs and the microtubules emanating from it (Kusch et al., 2002, 2003; Liakopoulos et al., 2003; Maekawa et al., 2003). This asymmetry ensures that only one SPB orients toward the bud, while the other spindle pole orients toward the mother cell. Direct interaction of Kar9 with the microtubule plus-end tracking protein (+TIP) Bim1 has been established by yeast two-hybrid, velocity sedimentation, coimmunoprecipitation, and size-exclusion chromatography experiments (Korinek et al., 2000; Lee et al., 2000; Miller et al., 2000). Furthermore, Kar9 also interacts with the +TIPs Stu2 and Bik1; however, the roles and modes of these interactions remain unclear (Moore et al., 2006; Moore and Miller, 2007). At astral microtubule plus ends, the Bim1-Kar9 complex binds Myo2 that moves along actin cables emerging either from the bud cortex (Yin et al., 2000; Hwang et al., 2003) or from the shmoo tip (Hwang et al., 2003; Sheltzer and Rose, 2009). Thereby the microtubules decorated with Kar9 and the SPB attached to them are pulled toward the bud tip during metaphase and toward the shmoo tip during mating. Because Bim1 binds the plus ends of all microtubules, it is unclear how the localization of Kar9 is restricted to the astral microtubules emanating from only one SPB in mitotic cells. Whatever the pathways involved in establishing the asymmetry of Kar9 distribution in mitosis, there is no need for an analogous pathway during mating, since the partner nuclei contain only one SPB each.

One layer of control of Kar9 localization involves its posttranslational regulation. During metaphase, Kar9 is subjected to phosphorylation by mitotic kinases Cdk1/Clb4 and Dbf2/20 (Liakopoulos et al., 2003; Maekawa and Schiebel, 2004; Moore and Miller, 2007) or to sumoylation by the SUMO ligases Siz1 and Siz2 (Leisner et al., 2008). Interestingly, nonmodifiable versions of Kar9 (i.e., ablation of the sites described so far in the literature; Moore and Miller, 2007) localize to astral microtubules emanating from both SPBs, suggesting that, in a normal situation, Kar9 becomes modified on the mother side of the spindle and that these modifications down-regulate its interaction with spindle pole– and astral microtubule–associated proteins. Accordingly, immunoprecipitation of Kar9 in cell cycle–synchronized cells indicates that the Kar9-Bim1 interaction is lowest when Cdk1 activity is highest, that is, during metaphase (Liakopoulos et al., 2003). In addition, phosphomimetic mutations have established that the addition of negative charges weakens the interaction of Kar9 with Stu2 (Moore and Miller, 2007). Thus Kar9 regulation during mitosis appears to ensure its asymmetric localization and function. Because the mitotic kinases regulating Kar9 are inactive during the G1 phase of the cell cycle, these observations suggest that the function of Kar9 is not the same during cell division and mating. Here we used a combination of biophysical, biochemi-

cal, and cell biological methods to dissect the Kar9-Bim1 interaction and its role in nuclear positioning throughout the life cycle of budding yeast.

RESULTS

Biophysical characterization of Bim1 and Kar9

To understand the molecular determinants of the Kar9-Bim1 interaction, we first used biophysical and biochemical methods to determine how Kar9 and Bim1 interact with each other. To this end, we first set out to characterize the individual behavior of the bacterially expressed and purified proteins (Supplemental Figure S1).

Like all EB1 proteins (reviewed in Slep, 2010), Bim1 contains an N-terminal calponin homology (CH) domain that binds microtubule plus ends, a central predicted flexible linker, and a C-terminal domain that binds +TIPs (Figure 1A). To characterize the oligomerization state of Bim1 in solution, we performed size-exclusion chromatography coupled to multiangle light scattering (SEC-MALS; allows the determination of molecular masses by measuring light-scattering intensities and concentrations of particles in solution) and analytical ultracentrifugation (AUC; allows the determination of molecular masses by measuring the sedimentation behavior of particles in solution) experiments (summarized in Table 1). SEC-MALS measurements of full-length Bim1 yielded a molecular mass of 80.7 kDa (Figure 1C), consistent with the formation of dimers (calculated molecular mass of the Bim1 dimer: 76.4 kDa). SEC-MALS measurements of the C-terminal domain of Bim1 (residues 194–344; denoted as Bim1C) resulted in a molecular mass of 34.8 kDa (Figure 1C), which is also consistent with the formation of dimers (calculated molecular mass of the Bim1C dimer: 33.6 kDa). To determine the stability of the Bim1 dimer, we performed sedimentation velocity and sedimentation equilibrium experiments of C-terminally green fluorescent protein–tagged Bim1 (Bim1-GFP) using a fluorescence-detection AUC system. At protein concentrations of 5–150 nM, Bim1-GFP sedimented as a single molecular species (Supplemental Figure S2A). Sedimentation equilibrium experiments of Bim1-GFP in the same concentration range yielded an averaged molecular mass consistent with the formation of dimers (Supplemental Figure S2B and Table 1). These results demonstrate that the C-terminal domain of Bim1, like those of its human orthologues EB1 and EB3 (Sen et al., 2013), mediates the formation of very stable Bim1 homodimers.

Next we characterized the biophysical and structural properties of Kar9. Secondary structure analysis of the Kar9 sequence predicts a high helical content for the first two-thirds of the protein (denoted as Kar9N; residues 1–429), while the last third of the protein (denoted as Kar9C; residues 429–644) is predicted to be largely unstructured (Figure 1B). To verify these predictions, we performed circular dichroism (CD) spectroscopy measurements with full-length Kar9, Kar9N, and Kar9C. The CD spectra of full-length Kar9 and Kar9N were characteristic of proteins containing a high helical content (Supplemental Figure S2C). In contrast, Kar9C revealed a CD spectrum characteristic of a largely unstructured protein (Supplemental Figure S1C). Both full-length Kar9 and Kar9N displayed a cooperative thermal unfolding profile that is indicative of a native-like structure (Supplemental Figure S2D). These results are consistent with the secondary structure analysis of Kar9, predicting a folded, predominantly helical N-terminal domain and a largely unstructured C-terminal domain for the protein.

The oligomerization state of Kar9 was assessed by SEC-MALS and AUC measurements (Table 1). SEC-MALS experiments at two different Kar9 concentrations (2 and 15 μM injected onto the SEC column) yielded major molecular masses of 83.1 and 106.8 kDa
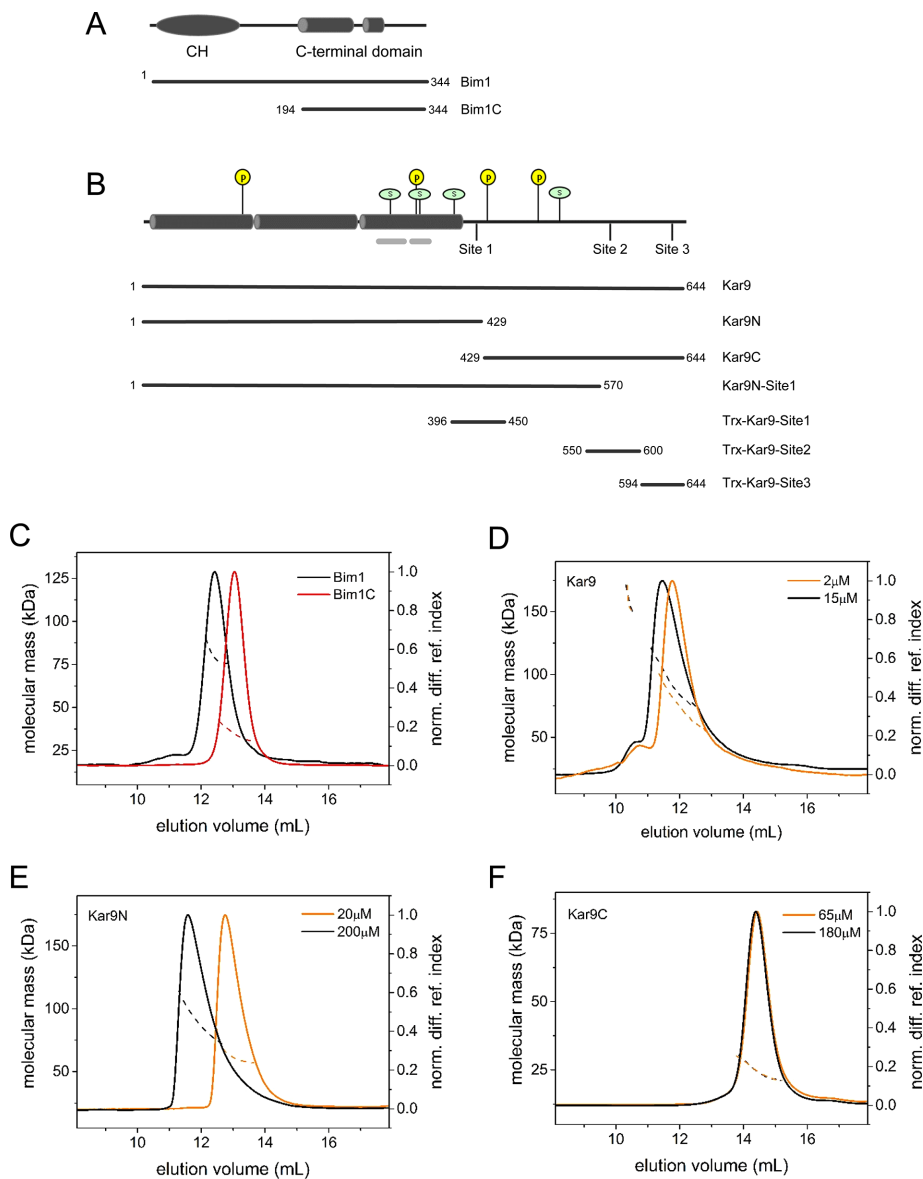
FIGURE 1: Overview of protein fragments and biophysical analysis of Bim1 and Kar9. (A, B) Schematic representation of the Bim1 (A) and Kar9 (B) constructs used in this study (indicated by black bars). In the schematic representations, the gray oval and cylinders indicate the CH domain and the helical regions of Bim1 and Kar9, respectively; black lines indicate disordered regions; P, known phosphorylation sites; S, known sumoylation sites of Kar9. Regions of Kar9 that potentially form coiled-coils are indicated with gray bars. Note that Trx-Kar9-Site1 was not fully soluble at the high concentrations needed to perform ITC experiments. (C) SEC-MALS chromatograms of Bim1 (black) and Bim1C (red). (D) SEC-MALS chromatograms of Kar9. The orange and black lines correspond to Kar9 injected at a concentration of 2 and 15 μM, respectively. (E) SEC-MALS chromatograms of Kar9N. The orange and black lines correspond to Kar9N injected at a concentration of 20 and 200 μM, respectively. (F) SEC-MALS chromatograms of Kar9C. The orange and black lines correspond to Kar9C injected at a concentration of 65 and 180 μM, respectively. SEC-MALS chromatograms were recorded by monitoring the differential refractive index of an injected sample and are represented as continuous, normalized traces. The dashed lines across SEC elution peaks correspond to the molecular masses determined by MALS. norm. diff. ref. index, normalized differential refractive index.

sedimentation velocity experiments revealed that Kar9 sediments as a single molecular species at low micromolar protein concentrations but populates additional larger molecular mass species at higher concentrations (Supplemental Figure S2E). To identify which part of Kar9 mediates its oligomerization, we performed SEC-MALS experiments with Kar9N and Kar9C. Analysis of Kar9N at 20 and 200 μM (concentration injected onto the SEC column) yielded molecular masses of 65.5 and 101.1 kDa, respectively (Figure 1E). This result suggests that Kar9N, like full-length Kar9, is monomeric at low micromolar concentrations (calculated molecular mass of the Kar9N monomer: 51.0 kDa) and displays the tendency to form dimers at higher concentrations. In contrast, SEC-MALS measurements of Kar9C at 65 and 180 μM resulted in similar molecular masses of 24.6 and 24.9 kDa, respectively (Figure 1F), consistent with the presence of monomers (calculated molecular mass of the Kar9C monomer: 25.9 kDa). These results suggest that Kar9 can self-associate via its N-terminal domain, in agreement with yeast two-hybrid and coimmunoprecipitation data (Miller *et al.*, 2000). Notably, residues 276–305 and 313–337 in the N-terminal domain of Kar9 are predicted to form coiled-coil structures that could be involved in Kar9 dimerization (Figure 1B).

Together these results establish that our bacterially produced Bim1 protein displays similar biophysical and structural properties to its mammalian orthologues: it forms dimers in solution, with the C-terminal domain mediating this homotypic interaction. Likewise, our bacterially produced Kar9 protein displays a structured helical N-terminal region and a disordered C-terminal part and shows the ability to self-associate via its N-terminal region.

Biophysical characterization of the Kar9-Bim1 interaction

Knowing the biophysical and structural properties of Bim1 and Kar9, we next investigated the molecular determinants of their interaction. To evaluate this, we first carried out fluorescence-detection sedimentation velocity experiments with mixtures of Kar9 and Bim1-GFP. As shown in Figure 2A, Bim1-GFP (5 nM) sedimented as a single molecular species. Addition of increasing amounts of Kar9 shifted the sedimentation peak to a higher sedimentation coefficient value compared with Bim1-GFP alone, indicating complex formation. A full shift of the sedimentation peak occurred already upon addition of 6.25 nM of Kar9. We therefore concluded that Kar9 binds Bim1-GFP with an affinity in the low nanomolar range. As a

(Figure 1D). This result suggests that Kar9 is monomeric at low micromolar concentrations (calculated molecular mass of the Kar9 monomer: 75.7 kDa) but displays the tendency to self-associate in a concentration-dependent manner. Consistent with this observation,

Protein	Calculated M_m of monomers (kDa)	Experimental M_m (kDa)	Method	Interpretation
Bim1	38.3	80.7	SEC-MALS	Dimer
Bim1C	16.9	34.8	SEC-MALS	Dimer
Bim1-GFP	65.6	129.5 ± 0.5[a]	Se AUC	Dimer
Kar9	75.7	83.1 (137.8[b])	SEC-MALS (2 µM[c])	Monomer-dimer
		106.8 (150.6[b])	SEC-MALS (15 µM[c])	
Kar9N	51.0	65.5	SEC-MALS (20 µM[c])	Monomer-dimer
		101.1	SEC-MALS (200 µM[c])	
Kar9C	25.9	24.6	SEC-MALS (65 µM[c])	Monomer
		24.9	SEC-MALS (180 µM[c])	
Bim1 + Kar9 (1:2)	38.8 + 75.7	162.4	SEC-MALS	1 Bim1 dimer + 1 Kar9 monomer
Bim1C + Kar9 (1:1)	16.9 + 75.7	131.8	SEC-MALS	1 Bim1C dimer + 1 Kar9 monomer
Bim1C + Kar9C (1:1)	16.9 + 25.9	55.9	SEC-MALS	1 Bim1C dimer + 1 Kar9C monomer
Bim1-GFP + Kar9 (1:4)	65.6 + 75.5	202 ± 1.3	Se AUC	1 Bim1 dimer + 1 Kar9 monomer
Bim1-GFP + Kar9 (1:10)		238 ± 1.6		

Se AUC, sedimentation equilibrium AUC. Fit to the data provided errors for the M_m values reported. Error estimation: $M_m \pm 10\%$.
[a]Global fit of equilibrium distributions of 50, 100, and 200 nM Bim1-GFP at rotor speeds of 8000 and 12,000 rpm.
[b]Molecular mass of the shoulder of the elution profile.
[c]Protein concentration injected onto the SEC column.

TABLE 1: Molecular masses (M_m) of proteins and complexes.

second method, we performed fluorescence correlation spectroscopy (FCS; allows us to measure binding isotherms by recording the increase in diffusion time upon complex formation) experiments with mixtures of Kar9 and Bim1-GFP and determined the diffusion time, τ, of the fluorescently labeled species in solution. As shown in Figure 3C, adding increasing amounts of Kar9 to Bim1-GFP (5 nM) caused the calculated diffusion time of the GFP signal to increase by a maximum factor of 1.15, which was stably reached at Kar9 concentrations of ~100 nM. The shape of the resulting binding isotherm suggests that Kar9 binds Bim1-GFP with an affinity in the low nanomolar range, consistent with the sedimentation velocity data (Table 2).

To determine the stoichiometry of the Kar9-Bim1 complex, we used SEC-MALS analysis of a mixture of Kar9 and Bim1, which yielded an averaged molecular mass of 162.4 kDa (Figure 2B), consistent with complex formation in the ratio of one Kar9 monomer to one Bim1 dimer (calculated molecular mass of the 1:2 stoichiometric Kar9-Bim1 complex: 152.3 kDa; Table 1). This result was confirmed by fluorescence-detection sedimentation equilibrium experiments (Supplemental Figure S2F and Table 1).

Next we sought to determine which parts of Kar9 and Bim1 interact with each other and therefore performed additional fluorescence-detection sedimentation equilibrium experiments with different protein fragments (Figure 2, C and D). Addition of increasing amounts of either Kar9 or Kar9C to Bim1-GFP or Bim1C-GFP shifted the corresponding sedimentation peaks to higher sedimentation coefficient values compared with Bim1 or Bim1C-GFP alone, indicating complex formation in all four cases. A full shift of the sedimentation peaks to stable sedimentation coefficient values occurred each time, already upon addition of 6.25 nM of either of the Kar9 variants. In contrast, we did not observe any complex formation between Kar9N (concentration range between 5 nM and 64 µM) and Bim1-GFP or Bim1C-GFP (5 nM) in the concentration range tested (Figure 2, C and D). SEC-MALS analysis of a mixture of Kar9C and

Bim1C yielded an averaged molecular mass in agreement with a complex consisting of one Kar9 monomer and one Bim1C dimer (Table 1).

Previous studies have shown that Kar9 is phosphorylated by the mitotic kinases Cdk1/Clb4 and Dbf2/Dbf20 at Ser-197, Ser-332, Ser-429, and Ser-496 (Liakopoulos et al., 2003; Maekawa and Schiebel, 2004; Moore and Miller, 2007; Hotz et al., 2012) and that Kar9 phosphorylation negatively regulates its interaction with Bim1 in vivo (Liakopoulos et al., 2003). However, how direct the effects of phosphorylation are on the Kar9-Bim1 interaction is unknown. To examine this question, we simultaneously mutated the above-mentioned serine residues and the alanine residue N-terminal to Ser-197 in Kar9 to glutamic acid to mimic phosphorylation (denoted as Kar9-5E; the double mutation at position 196 and 197 of Kar9 was intended to increase the negative charge at this particular phosphorylation site; Moore and Miller, 2007). Sedimentation velocity experiments revealed that Kar9-5E displays similar oligomerization properties to wild-type Kar9 (unpublished data), while FCS experiments showed that, like the wild-type Kar9, the Kar9-5E binds Bim1-GFP with an affinity in the low nanomolar range (Table 2).

Together these results demonstrate that bacterially produced Kar9 and Bim1 can form a very stable complex in solution and that tight interaction between Kar9 monomers and Bim1 dimers is primarily mediated by the C-terminal domains of the proteins. They further suggest that the role of phosphorylation of the currently known serine residues in Kar9 might not be to directly regulate the stability and/or stoichiometry of the Kar9-Bim1 complex.

Molecular determinants of the Kar9-Bim1 interaction

Because the interaction of Kar9 with Bim1 was restricted to their respective C-terminal parts, we used synthetic peptide arrays on cellulose membrane supports (SPOT; Wenschuh et al., 2000; Frank, 2002; Volkmer, 2009) to identify the Bim1-binding sites in Kar9. We generated an array of peptides with a length of either 15 or
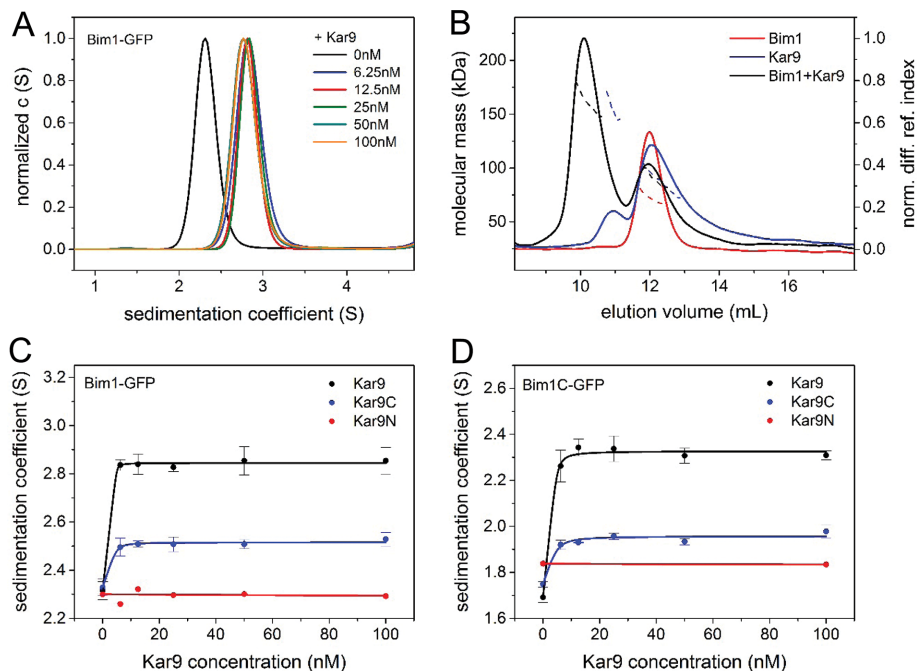
FIGURE 2: Biophysical analysis of the Kar9-Bim1 complex. (A) Normalized continuous distribution, c (S), of sedimentation coefficients, S, for 5 nM Bim1-GFP (black, sedimentation coefficient 2.3 S) mixed with different concentrations of Kar9 (6.25–100 nM; blue to orange, sedimentation coefficient 2.8 S) measured by fluorescence AUC. (B) SEC-MALS chromatograms of Kar9 (blue), Bim1 (red), and mixtures of Kar9 and Bim1 (1:2 M ratio; black) recorded by monitoring the differential refractive index of an injected sample and represented as continuous, normalized traces. Dashed lines across SEC elution peaks correspond to molecular masses determined by MALS. (C, D) Measured sedimentation coefficients of the Bim1-GFP (C) and Bim1C-GFP (D) signals plotted against Kar9 concentrations. Symbols represent the measured data (Kar9, black; Kar9C, blue; and Kar9N, red), and lines represent fits to the data. For measurements with Kar9 and Kar9C, the data represent the mean of at least two independent measurements; error bars represent SDs. For measurements with Kar9N, no change in sedimentation behavior was observed for concentrations up to 64 μM Kar9N. Sedimentation coefficients: Bim1-GFP, 2.3 S; Bim1C-GFP, 1.7 S, Bim1-GFP-Kar9, 2.8 S; Bim1-GFP-Kar9C, 2.5 S; Bim1C-GFP-Kar9, 2.3 S; and Bim1C-GFP-Kar9C, 2.0 S. norm. diff. ref. index, normalized differential refractive index.

24 amino acid residues and shifted in register by three amino acids to scan almost the entire C-terminal half of Kar9 (amino acid segment 373–644). The array was subsequently incubated with a solution of 6xhistidine-tagged Bim1 (His-Bim1), washed, and developed with an antipolyhistidine antibody. Peptides that interacted with Bim1 appeared as black spots of variable intensities on the membrane. As shown in Figure 3A, three positive regions in the peptide array were revealed: the first region spanned amino acids 406–426 (denoted as Site1), the second region spanned amino acids 565–585 (denoted as Site2), and the third region spanned amino acids 613–633 (denoted as Site3).

Next we sought to investigate which sequence determinants in the three Kar9 sites mediate the interaction of Kar9 with Bim1. Notably, Site1 and Site2 contain an SxIP-like (KKIP) and a canonical SxIP (SRIP) motif, respectively (Figure 3A). Such motifs are well established to mediate binding of many diverse +TIPs to the C-terminal cargo-binding domain of EB1 family members (Honnappa et al., 2009; Buey et al., 2012; Jiang et al., 2012). In contrast, inspection of the sequence of Site3 did not reveal any obvious EB1-binding motif (Figure 3A). To test whether Site1, Site2, and Site3 are functional, we fused 50 amino acid peptides, centrally containing the respective sites, to the C-terminus of thioredoxin (denoted as Trx-Kar9-Site1,

Trx-Kar9-Site2, and Trx-Kar9-Site3; Figure 1B) and sought to use isothermal titration calorimetry (ITC; allows measuring binding isotherms by recording the heat change occurring upon complex formation) to assess the binding activities of these recombinant fusion proteins to Bim1C, as described previously (Buey et al., 2012). Because Trx-Kar9-Site1 was not fully soluble at the high concentrations needed to perform the ITC experiments, we instead produced a fragment containing the first 570 N-terminal residues of Kar9 (denoted as Kar9N-Site1; Figure 1B), and used FCS to determine its binding activity to Bim1-GFP.

As shown in the inset of Figure 3B and summarized in Table 2, titration of increasing amounts of Kar9N-Site1 into a Bim1-GFP solution yielded a binding isotherm, suggesting an equilibrium dissociation constant, K_d, in the 100 μM range. This result can be explained by the presence of a lysine residue at position 1 of the Site1 SxIP-like motif KKIP, which is expected to be unfavorable for stable EB1 binding (Honnappa et al., 2009; Buey et al., 2012). In contrast to Kar9N-Site1, Trx-Kar9-Site2 bound Bim1C with a K_d of 0.12 ± 0.02 μM and a stoichiometry number, n, of 1 (monomer Trx-Kar9-Site2:monomer Bim1C). This result is consistent with the formation of a complex consisting of two Trx-Kar9-Site2 monomers and one Bim1C dimer. Simultaneous mutation of the isoleucine-proline dipeptide of the SxIP motif of Site2 to asparagines (Ile575Asn, Pro576Asn; Trx-Kar9-Site2mut) completely abrogated binding of the Trx-Kar9-Site2 mutant to Bim1C (Figure 3B). This result demonstrates the functional relevance and canonical nature of the SxIP motif in Site2 of Kar9 (Honnappa et al., 2009; Buey et al., 2012; Jiang et al., 2012). As shown in Figure 3B, Trx-Kar9-Site3 bound to Bim1C with a K_d of 0.56 ± 0.11 μM and an n value of 1 (monomer Trx-Kar9-Site3:monomer Bim1C). To pinpoint possible critical residues in Site3, we analyzed a sequence alignment of Site3 across Kar9 paralogues from different budding yeasts (unpublished data). On the basis of sequence conservation and context, we decided to simultaneously mutate Pro-624 and Thr-625 to alanine in Trx-Kar9-Site3 (Trx-Kar9-Site3mut) and tested the impact of these mutations on complex formation with Bim1C. As shown in Figure 3B, binding of Trx-Kar9-Site3mut to Bim1C was abrogated, demonstrating the functional relevance of Site3 residues Pro-624 and Thr-625 for Bim1 binding.

To test the activity of the three Bim1-binding sites in the context of full-length Kar9, we produced two Kar9 variants in which we either concomitantly mutated Site2 and Site3 (Ile575Asn, Pro576Asn, Thr625Ala, Pro626Ala; from here onward denoted as Kar9-100 to mark that Site1 is intact and the Site2 and Site3 are absent; the wild-type protein in this notation would correspond to Kar9-123 but will remain referred to as Kar9) or all three sites (Ile416Asn, Pro417Asn, Ile575Asn, Pro576Asn, Thr625Ala, Pro626Ala; denoted as Kar9-000). The affinities of the Kar9 mutants for Bim1-GFP and Bim1C-GFP

Site 1: 406-SNKIATSKKKKIPKPKSLGFGR-426
Site 2: 565-WNHYRSLPSRIPIYKDKVVKV-585
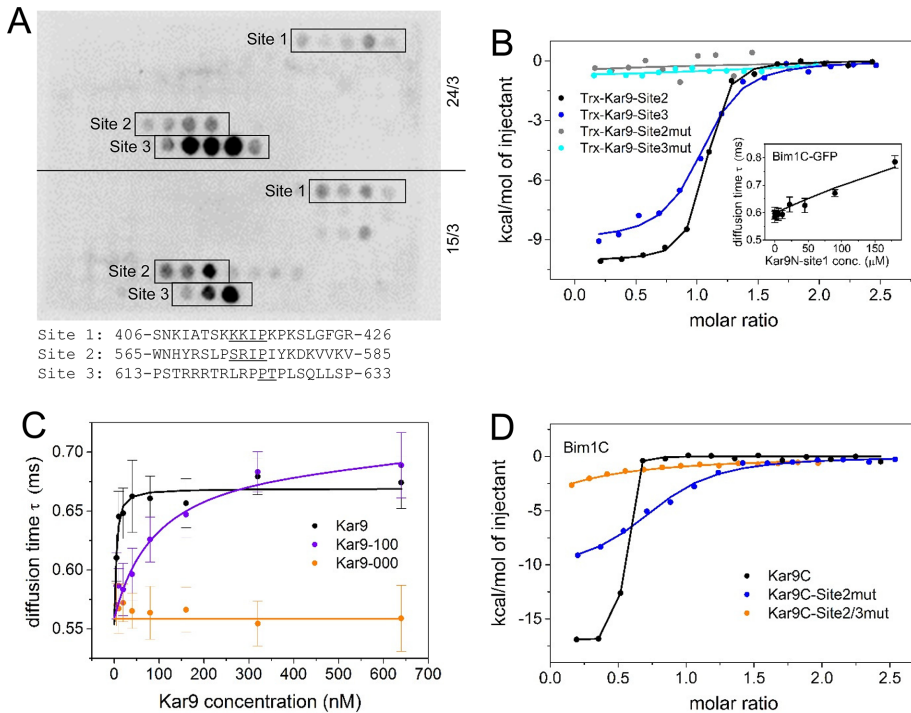Site 3: 613-PSTRRRTRLRPPTPLSQLLSP-633

FIGURE 3: Characterization of Kar9 Site1, Site2, and Site3 for Bim1 binding. (A) Peptide arrays for Kar9 segment 373–644 using 15 or 24 amino acid peptides that are shifted in register by three amino acids. The arrays contain 84 peptides in the case of the 24-mers and 87 peptides in the case of the 15-mers (for more details, see Supplemental Tables S1 and S2). The three positive peptide hit regions that were consistently revealed in both arrays are boxed and labeled as Site1, Site2, and Site3. Bottom: amino acid sequences of Site1, Site2, and Site3. The SxIP motifs in Site1 and Site2 and the two residues in Site3 that were identified as critical for binding Bim1 are underlined. (B) Binding isotherms determined by ITC for the complexes formed between Bim1C and Trx-Kar9-Site2 (black), Trx-Kar9-Site3 (blue), Trx-Kar9-Site2mut (gray), or Trx-Kar9-Site3mut (light blue). Each data point represents the integrated heat change (in kcal/mol) for a single injection and at a distinct molar ratio of Kar9:Bim1. Inset: Binding isotherm determined by FCS for the complex formed between Bim1C-GFP and Kar9N-Site1. Each data point corresponds to the diffusion time of a GFP particle and at a distinct molar ratio of Kar9:Bim1. (C) Binding isotherms determined by FCS for the complexes formed between Bim1-GFP and Kar9 (black), Kar9-100 (purple), or Kar9-000 (yellow). Data points correspond to average ± SD ($n = 10$). (D) Binding isotherms determined by ITC for the complexes formed between Bim1C and Kar9C (black), Kar9C-Site2mut (blue), or Kar9-Site2/3mut (yellow).

Bim1C dimer (Figure 3D and Table 2). The affinity of Kar9C-Site2mut was strongly reduced by three orders of magnitude compared with wild-type Kar9C ($K_d = 4.7 \pm 0.9$ μM), while n increased to a value close to 1, consistent with the formation of a complex consisting of two Kar9C-Site2mut monomers and one Bim1C dimer (Figure 3D). Binding of the double-mutant Kar9C-Site2/3mut to Bim1C was essentially abrogated (Figure 3D).

Taken together, these results establish three distinct Bim1-binding sites in the C-terminal part of Kar9, one having low affinity (Site1) and two presenting high affinities (Site2 and Site3). They further suggest that Site1 is only fully functional in the context of full-length Kar9 and that Site2 and Site3 can cooperate by simultaneously interacting with one Bim1 dimer to mediate stable complex formation between the two proteins.

In vitro reconstitution of microtubule-tip tracking by Kar9

To test whether the Kar9-Bim1 interaction is necessary and sufficient for Kar9 to track growing microtubule plus ends, as observed in *Saccharomyces cerevisiae* cells (Liakopoulos *et al.*, 2003; Maekawa and Schiebel, 2004), we sought to reconstitute the microtubule-Bim1-Kar9 interaction network using an in vitro assay based on total internal reflection fluorescence microcopy (TIRF; Bieling *et al.*, 2007; Montenegro Gouveia *et al.*, 2010). In contrast to a previous study (Zimniak *et al.*, 2009), in our hands the assay did not produce robust and specific microtubule-tip localization of Bim1-GFP under the experimental conditions reported, primarily due to the tendency of the bacterially produced protein to form aggregates on the cover slide (unpublished data). We thus changed our experimental layout and switched to the fission yeast *Schizosaccharomyces pombe* EB1 family member Mal3, which was successfully used by several researchers in the past (Bieling *et al.*, 2007; Katsuki *et al.*, 2009). In contrast to Bim1-GFP, Mal3-GFP displayed robust microtubule plus-end tracking activity in our in vitro reconstitution assay (Figure 4A). Under the same conditions, Kar9-GFP alone was not able to autonomously track growing microtubule plus ends (unpublished data). However, upon addition of unlabeled Mal3, we obtained robust microtubule plus-end localization of Kar9-GFP (Figure 4B).

To assess the effect of the Kar9-Mal3 complex on microtubule dynamics, we determined the growth speed (v_{growth}), shrinkage speed (v_{shrink}), and catastrophe frequency (f_{cat}) of individual microtubule plus ends at 37°C and at a tubulin concentration of 10 μM; under the conditions used, we hardly observed rescue events, and thus the rescue frequency (f_{res}) was not determined. As summarized in Table 3, v_{growth} was not significantly affected by Mal3-GFP alone, while at concentrations of 100 nM, the protein reduced v_{shrink} by a factor of ~1.7 and increased f_{cat} by a factor of ~2.3, values that are

were subsequently assessed by FCS. As shown in Figure 3C, the Kar9-100 displayed a K_d of 95 ± 26 for Bim1-GFP and a K_d of 230 ± 99 nM for BimC-GFP (see also Table 2). In contrast, no binding of Kar9-000 to Bim1-GFP and Bim1C-GFP was observed up to a Kar9-000 concentration of 5 μM.

Notably, the Kar9C fragment that we used in our previous experiments (see above) contains only Site2 and Site3, which are separated by roughly 50 amino acids (Figure 1A). It is known that SxIP motifs arranged in tandem and separated by a few tens of residues can strongly increase the affinity of a polypeptide fragment for the C-terminal domain of EB1 (Buey *et al.*, 2012). To assess whether Site2 and Site3 of Kar9 can cooperate with respect to Bim1 binding, we introduced mutations in Kar9C. To this end, we mutated either Site2 alone (same mutations as for Trx-Kar9-Site2mut; denoted as Kar9C-Site2mut), or Site2 and Site3 simultaneously (same mutations as for Kar9-100; denoted as Kar9C-Site2/3mut). In agreement with our MALS and AUC data (Table 1), ITC experiments with wild-type Kar9C and Bim1C yielded a K_d of 9.1 ± 4.9 nM and an n value close to 0.5 (monomer Kar9C:dimer Bim1C), consistent with the formation of a tight complex consisting of one Kar9C monomer and one

Protein	K_d	n	Method
Bim1-GFP + Kar9	Low nM[a]	—	Sv AUC
Bim1-GFP + Kar9N	No binding	—	Sv AUC
Bim1-GFP + Kar9C	Low nM[a]	—	Sv AUC
Bim1C-GFP + Kar9	Low nM[a]	—	Sv AUC
Bim1C-GFP + Kar9N	No binding[b]	—	Sv AUC
Bim1C-GFP + Kar9C	Low nM[a]	—	Sv AUC
Bim1-GFP + Kar9-5E	Low nM[b]	—	FCS
Bim1C + Trx-Kar9-Site1	Not determined[c]	—	ITC
Bim1C + Trx-Kar9-Site2	0.12 ± 0.02 µM	0.99 ± 0.01	ITC
Bim1C + Trx-Kar9-Site2mut	No binding[b]	—	ITC
Bim1C + Trx-Kar9-Site3	0.56 ± 0.11 µM	0.99 ± 0.02	ITC
Bim1C + Trx-Kar9-Site3mut	No binding[b]	—	ITC
Bim1-GFP + Kar9N-Site1	Not determined[c]	—	FCS
Bim1C-GFP + Kar9N-Site1	Not determined[c]	—	FCS
Bim1-GFP + Kar9	Low nM[b]	—	FCS
Bim1-GFP + Kar9-100	94.5 ± 26.4 nM	—	FCS
Bim1-GFP ± Kar9-000	No binding[b]	—	FCS
Bim1C-GFP + Kar9	4.5 ± 0.4 nM	—	FCS
Bim1C-GFP + Kar9-100	230 ± 99 nM	—	FCS
Bim1C-GFP + Kar9-000	No binding[b]	—	FCS
Bim1C + Kar9C	9.1 ± 4.9 nM	0.48 ± 0.01	ITC
Bim1C + Kar9C-Site2mut	4.7 ± 0.9 µM	0.74 ± 0.03	ITC
Bim1C + Kar9C-Site2/3mut	Not determined[c]	—	ITC

K_d, equilibrium dissociation constant; n, stoichiometry number; s, sedimentation coefficient; Sv AUC, sedimentation velocity AUC. FCS fit to the data provided errors for the K_d values reported. ITC fit to the data provided errors for the K_d and n values reported.

[a]A full shift of the sedimentation peak to a stable sedimentation coefficient value was obtained upon addition of 6.25 nM of the Kar9 variant to 5 nM of the Bim1-GFP variant.
[b]No binding in the concentration range tested.
[c]Data could not be subjected to rigorous analysis; however, the shape of the binding isotherm suggests that the K_d value is in the high micromolar range. In the case of Trx-Kar9-Site1, we could not perform the ITC experiment because this construct was not fully soluble at the high concentrations.

TABLE 2: Equilibrium dissociation constants of protein complexes.

in reasonable agreement with a previous report (Bieling et al., 2007). Experiments in the presence of the Mal3-Kar9-GFP complex (250 and 100 nM for Mal3 and Kar9-GFP, respectively) yielded microtubule plus-end dynamics parameters similar to those seen with Mal3-GFP alone (Table 3). These results demonstrate that Kar9 and Mal3 can form a functional microtubule tip–tracking complex in vitro. They further revealed that microtubule tip–localized Kar9 does not significantly affect microtubule dynamics under the experimental conditions tested.

Either Site2 or Site3 of Kar9 is sufficient to promote Kar9 localization and function during mating

Given the behavior of the Kar9-Bim1 complex in solution and the way that the different Kar9 sites contribute to Bim1 binding, we next tested the roles of Site1, Site2, and Site3 in living cells. In a first set of experiments, we sought to investigate how mutation of the different sites affects nuclear positioning during pheromone arrest and cellular mating. To this end, we treated mutant and control cells (MATa) with the alpha-factor pheromone and used cellular markers to visualize the mitotic apparatus (cyan fluorescent protein [CFP]-Tub1) and Kar9 localization (the Kar9 alleles were labeled with three copies of the superfolder GFP, Kar9*-3xsfGFP). The data showed that there was a strong correlation between the ability of Kar9 alleles to bind cytoplasmic microtubules and to correctly move the nucleus toward the shmoo tip (Figure 5, A and B). In this respect, both the Kar9-020 (I416N P417N P624A T625A) and Kar9-003 (I416N P417N I575N P576N) mutants behaved and functioned very similarly to the wild-type protein. In contrast, Kar9-100 (I575N P576N P624A T625A) and Kar9-000 (I416N P417N I575N P576N P624A T625A) failed to localize, and the nucleus was randomly positioned within the shmooing cell, as in kar9Δ mutant cells. Thus Bim1 binding is necessary for Kar9 function during nuclear positioning. Furthermore, each of Site2 and Site3, but not Site1, was sufficient to ensure a functional Kar9 during pheromone arrest.

Successful mating requires that the nuclei migrate further toward each other and undergo karyogamy upon cell fusion. To address whether the Kar9-Bim1 complex also contributes to this process, we mixed yeast cells of opposite mating types, which carry a Kar9 allele labeled with GFP. In addition, these cells carried nuclear markers to visualize conjugation, the movement of the parental nuclei toward each other, and their fusion into a larger diploid nucleus. To this end, we mated yeast cells expressing identical Kar9 alleles, one carrying GFP-labeled nuclear pores (Nup82-3xsfGFP), while the other expressed Cdc28 fused to 3xmKate, and imaged them using time-lapse microscopy. Cdc28-3xmKate labeled the nucleoplasm. Because both proteins showed some cytoplasmic background staining, sudden mixing of these green and red signals identified the time at which cell fusion took place. In the fused cells, both nuclei were rapidly visible in the red channel due to Cdc28-3xmKate being readily imported into the nucleoplasm of the partner cell. When it took place, karyogamy was clearly evidenced by the sudden and rapid flux of green nuclear pores between the labeled nucleus and its partner and the subsequent dissolution of both these nuclei into a single larger one (Figure 5C). We used our time-lapse recordings to assess the status of the partner nuclei 40 min after cell fusion. At that time point, virtually all zygotes of wild-type partners had completed karyogamy. Remarkably, either Site2 or Site3 of Kar9 was individually sufficient for karyogamy. In contrast, cells expressing Kar9-100 or lacking Kar9 altogether showed a greater proportion of zygotes with nuclei that had successfully congressed but failed to fuse (Site1+: 34.18% ± 18.27% vs. kar9Δ: 30.59% ± 7.24%). Both strains also showed an enlarged fraction of zygotes in which the nuclei were still far apart (kar9-100: 16.86% ± 9.18% vs. kar9Δ: 41.57% ± 14.49%).

Surprisingly, cells expressing Kar9-000 (lacking all three Bim1-binding sites) showed a milder phenotype (65.86% ± 18.06% fused
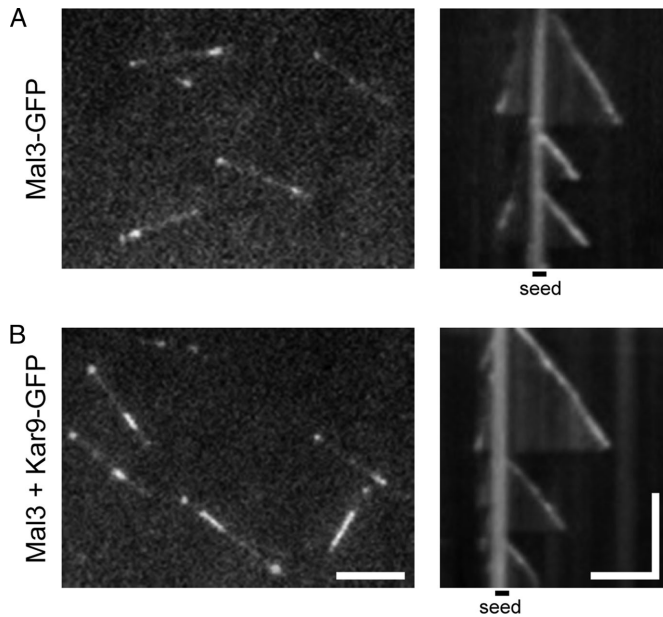
FIGURE 4: In vitro reconstitution of Mal3-dependent microtubule-tip tracking of Kar9. (A) Kymograph of Mal3-GFP showing that the protein tracks growing microtubule ends in vitro. (B) Kymograph of Kar9-GFP showing that the protein tracks growing microtubule ends in the presence of unlabeled Mal3. Single frames are shown on the left. The right panels depict exemplary kymographs. Plus ends point to the right side. Vertical scale bar: 120 s; horizontal scale bar: 5 μM.

nuclei and 20.19% ±11.38 juxtaposed nuclei) than either the *kar9Δ* (27.33% ± 14.47% fused nuclei) or *kar9-100* mutant cells (48.95% ± 15.53% fused nuclei). This result suggests that Kar9 function in karyogamy is at least in part independent of its ability to bind Bim1. Taking the results together, Kar9 function in karyogamy requires that either Site2 or Site3 be intact, in which case nuclear movement and fusion takes place with very similar efficiencies compared with what is observed in the mating of wild-type partners. However, much of the karyogamy process, but not congression, did not require Kar9 to interact with Bim1 and to localize to microtubules. Strikingly, in the absence of Site2 and Site3, Site1 was unable to promote congression. Furthermore, inactivation of Site1 to form Kar9-000 improved karyogamy, compared with the zygote expressing only Kar9-100. These data suggest that Site1 is involved in some inhibition of Kar9 function, at least during mating.

Site3 of Kar9 is inactive in metaphase cells
To assess the function of Kar9 during vegetative growth, we characterized the position of the spindle (CFP-Tub1) relative to the mother–bud neck (Figure 6A) and the alignment of the spindle along the mother–bud axis (Figure 6B) in metaphase cells, that is, in

cells with a spindle of 1–2 μm in length. The distance, d, from the middle of the spindle to the bud neck was standardized relative to the total length, L, of the mother cell and plotted (Figure 6A). Plotting the fraction of the cells in which the prolonged axis of the spindle passed through the width of the bud neck provides a measure of the efficacy of spindle alignment in the tested strains (Yin *et al.*, 2000) (Figure 6B). Any mutation affecting Site2, alone or in combinations with inactivation of the other Bim1-binding sites of Kar9 (*kar9-103* (I575N P576N), *kar9-003*, *kar9-100* and *kar9-000*), resulted in a phenotype similar to that of the Kar9-deleted mutant cells (*kar9Δ*), in which the spindles are randomly positioned within the mother cell during metaphase (Figure 6A). In contrast, individual or combined mutation of Site1 and Site3 did not perturb this process significantly. Thus Site2 plays a paramount role in Kar9 function during metaphase. In stark contrast to its role during mating, Site3 does not contribute to the metaphase function of Kar9 (Figure 6, A and B).

Consistent with this interpretation, the *kar9-103*, *kar9-003*, *kar9-100*, and *kar9-000* mutations, but not the *kar9-023* (I416N P417N), *kar9-120* (P624A T625A), and *kar9-020* were synthetic lethal with the dynein delete mutation (*dhc1Δ*), like the *kar9Δ* null mutation (Figure 6C). Notably, the dynein motor takes over spindle positioning function from Kar9 at anaphase onset and thereby corrects the spindle alignment defect and promotes the viability of the *kar9Δ* mutant cells. As a consequence, while individual inactivation of either of these pathways is not lethal, owing to the presence of either, cells do not survive the simultaneous inactivation of the two spindle-positioning pathways (Miller and Rose, 1998; Heil-Chapdelaine *et al.*, 2000). Together these genetic data establish that, in vegetative proliferating cells, Site2 is the only Bim1-binding site in Kar9 that is necessary and sufficient for Kar9 function in spindle positioning.

Site2 of Kar9 plays a preponderant role in Kar9 localization to the mitotic spindle
To better understand the molecular basis for the different involvements of the Bim1-binding sites in Kar9 during metaphase, we next characterized their role in Kar9 localization during vegetative proliferation. As documented previously (Kusch *et al.*, 2002; Liakopoulos *et al.*, 2003), in wild-type metaphase cells, Kar9 localizes asymmetrically to the side of the spindle that is proximal to the bud (Figure 7A). Inactivation of either Site1 or Site3 did not perturb this localization (Figure 7A). In contrast, mutating only Site2 resulted in the loss of Kar9 localization to the spindle asters of metaphase cells. In these cells, Kar9-103-3xsfGFP showed a dispersed localization throughout the bud cortex, referred to as the "green buds" phenotype (Figure 7A). Analysis of cells in which Kar9 kept only one of its Bim1-binding sites intact, that is, expressing Kar9-100-3xsfGFP, Kar9-020-3xsf-GFP, or Kar9-003-3xsfGFP alone, showed that only Kar9-020 localized correctly, whereas the other two proteins localized to the bud cortex but not to microtubule tips. Thus Site2 was necessary and

	V_{growth} (μm/min)	V_{shrink} (μm/min)	f_{cat} (min^{-1})	f_{res} (min^{-1})	#MT
Control	2.2 ± 0.4 (129)	119.8 ± 57.6 (43)	0.12 ± 0.17 (46)	n.d. (0)	123
Mal3-GFP	2.2 ± 0.4 (422)	72.0 ± 33.7 (284)	0.28 ± 0.16 (422)	n.d. (4)	253
Kar9-GFP	2.4 ± 0.3 (409)	78.2 ± 36.3 (258)	0.33 ± 0.16 (422)	n.d. (6)	226

Numbers in parentheses indicate number of events. Control, tubulin only. #MT, total number of microtubules analyzed. Values are given together with their corresponding SDs.

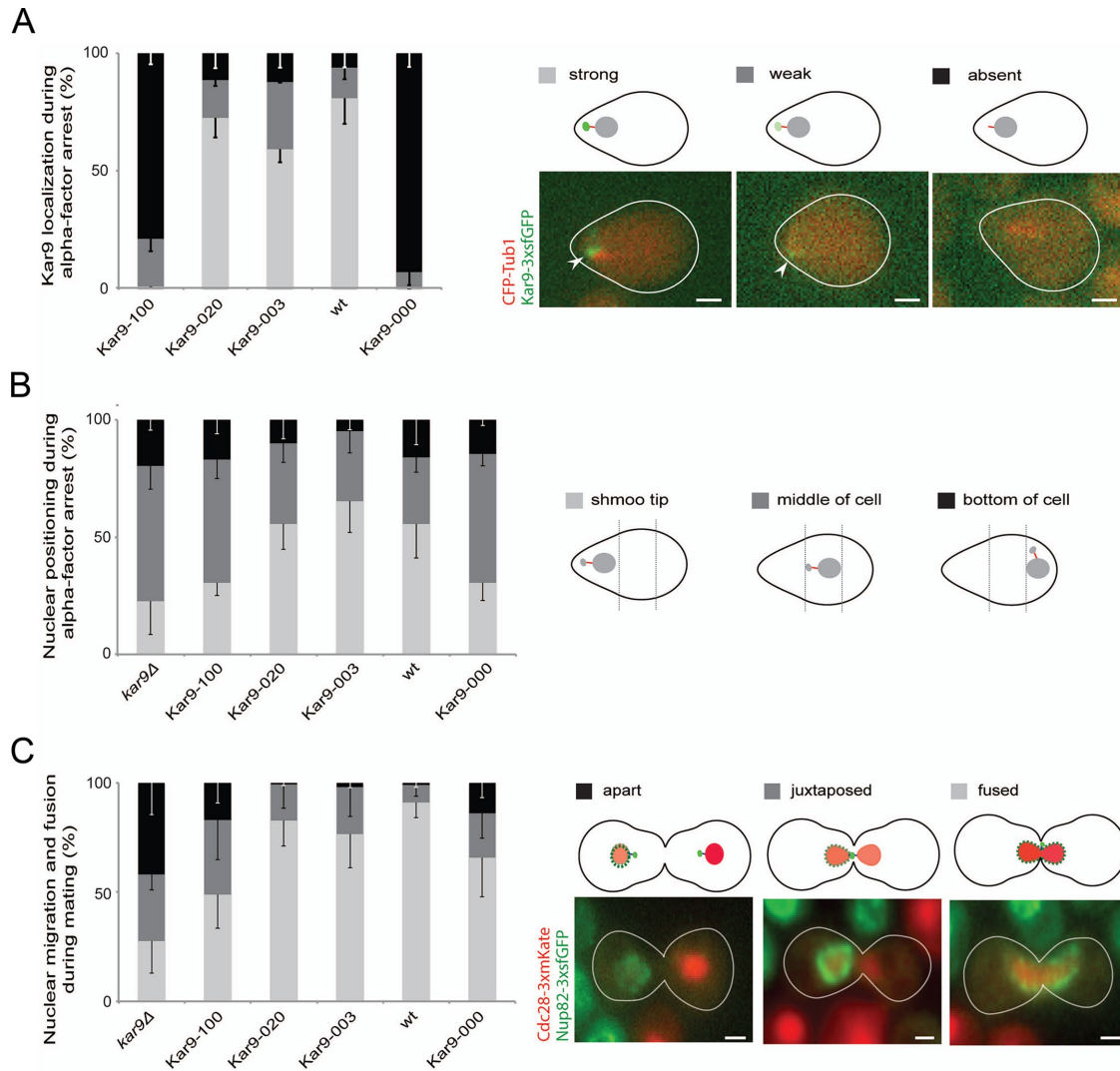**TABLE 3:** In vitro microtubule dynamics parameters.

FIGURE 5: Either Site2 or Site3 is sufficient to promote Kar9 localization and function during mating. (A) Kar9 localization as strong foci, weak foci, or absent, and its quantification during alpha-factor arrest in Kar9-100, Kar9-020, Kar9-003, wild type (wt), and Kar9-000 cells (mean value ± SD of three independent clones; *n* > 305 cells). White arrowheads point to the Kar9 foci localized on the half-spindle. Scale bar: 1.5 µm. (B) Quantification of the positioning of the half-spindle relative to the shmoo tip during alpha-factor arrest in *kar9Δ*, Kar9-100, Kar9-020, Kar9-003, wild type, and Kar9-000 cells (mean value ± SD of three independent clones; *n* > 305 cells per strain). (C) Quantification of nuclear positioning and fusion (apart, juxtaposed, and fused) during mating in *kar9Δ*, Kar9-100, Kar9-020, Kar9-003, wild type, and Kar9-000 cells (mean value ± SD of three independent crosses; *n* > 277 zygotes per strain). Partner nuclei were labeled in the mating cells with either Cdc28-3xmKate or Nup83-3xsfGFP to visualize conjugation, nuclear migration, and karyogamy. Scale bar: 1.5 µm.

sufficient for Kar9 to localize properly in metaphase cells. Site1 and Site3 seemed inactive in these cells, explaining why they failed to promote proper spindle positioning during metaphase (Figure 6, A and B).

Strikingly, however, despite its failure to localize to microtubule tips during metaphase, *kar9-103* (lacking only Site2) localized properly to the tip of cytoplasmic microtubules in both anaphase and G1-phase cells. The same was true for Kar9-003-GFP but not for Kar9-100-GFP and Kar9-000-GFP, which were mislocalized throughout the cell cycle (Figure 7B). These data corroborate our observation that Site3 is active in G1-arrested cells and during mating. They further suggest that some regulatory events inactivate Site3 specifically during metaphase. Such a regulation would explain why Site2 becomes indispensable for Kar9 function during mitosis. Our data

also indicate that, unlike for mating, Kar9 function in spindle positioning during mitosis strictly relies on its ability to bind Bim1.

Taken together, our analyses establish that, while Site1 does not seem to play any major role in Kar9 function during mating and vegetative proliferation, it might have an inhibitory effect on Kar9 function during mating. In contrast, Site3 contributes together with Site2 in Kar9 function during mating and is somehow inactivated during mitosis. At that stage, Site2 appears to be the only Bim1-binding site to be active in Kar9 and is therefore crucial for the metaphase function of Kar9.

DISCUSSION

Our biochemical and biophysical data establish that bacterially produced Kar9 and Bim1 form a tight and active microtubule plus-end
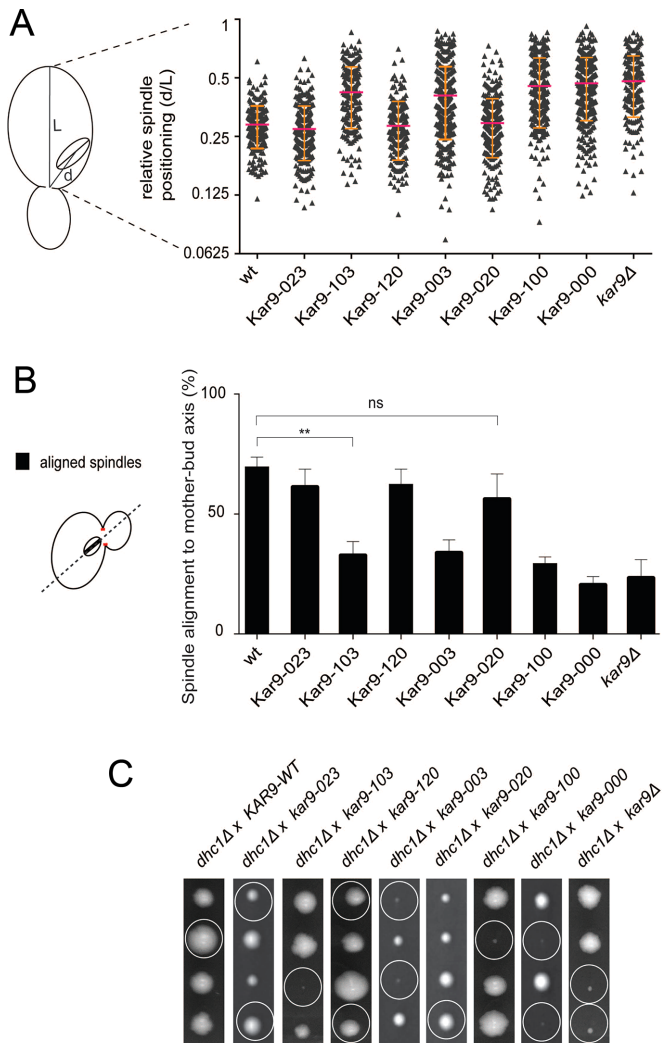
FIGURE 6: Site3 of Kar9 is inactive in metaphase cells. (A) Relative positioning of the mitotic spindle within the mother cell (d/L; $d =$ spindle to bud-neck distance; $L =$ the length of the mother cell) in yeast strains expressing various *Kar9* alleles. The data of three independent clones ($n > 186$ cells per strain) are represented as scattered dot plots, showing the mean value (magenta) ± SD (orange). The y-axis is in log2 scale. (B) Percentage of aligned spindles in metaphase cells bearing the specified Kar9 alleles. Same cells ($n > 186$ cells per strain) were quantified as shown in Figure 7A, including *kar9Δ* clones. The mean ± SD of three independent clones was plotted. Stars indicate the *p* value ($p = 0.0057$) obtained from unpaired *t* test compared with wild type. (C) Tetrad analysis from crosses of Kar9 alleles (as specified) and dynein delete (*dhc1Δ*). Circles denote the spores containing *dhc1Δ* combined with the specified Kar9 allele (> 7 tetrads observed, with an average of five double mutants per cross).

tracking complex composed of one Kar9 monomer and one Bim1 dimer. This finding is in contrast to previous results suggesting that only sumoylated Kar9 interacts with Bim1 (Huls *et al.*, 2012). One possible explanation for this discrepancy is the use of different protein expression and purification schemes and buffer systems and the general handling of the recombinantly expressed Kar9 protein samples. Moreover, the previous interaction data were obtained based on pull-down experiments, while here we used a combination of quantitative biophysical methods, including SEC-MALS, AUC, FCS, and ITC. Our data clearly show that bacterially produced

Kar9 and Bim1 form a very tight complex that involves three distinct Bim1-binding sites in Kar9, which we refer to as Site1, Site2, and Site3, and the C-terminal dimerization domain of Bim1. Our finding that the Kar9-Bim1 complex is very stable might explain why pull-down experiments require sumoylation of Kar9 for Kar9 interaction with bacterially expressed Bim1 in yeast extracts (Huls *et al.*, 2012). In such a situation, the bacterially expressed Bim1 that was introduced in yeast extracts might only very inefficiently displace the endogenous Bim1, thus hampering its ability to interact with the endogenous Kar9. Along these lines of reasoning, posttranslational modifications such as sumoylation might actually weaken the interaction between Kar9 and Bim1 to allow exchange rather than being required for the formation of the Kar9-Bim1 complex in the first place.

Besides sumoylation, Kar9 is also phosphorylated on at least four serine residues (Ser-197, Ser-332, Ser-429, and Ser-496) by the Cdk1/Clb4 and Dbf2/Dbf20 mitotic kinases, and it has been suggested that phosphorylation of Kar9 negatively regulates Kar9 interaction with Bim1 in vivo (Liakopoulos *et al.*, 2003; Maekawa and Schiebel, 2004; Moore and Miller, 2007; Hotz *et al.*, 2012). Here we showed that a Kar9 phosphomimetic mutant, in which all four known serine residues were simultaneously mutated to glutamic acid, bound Bim1 with a similar low-nanomolar affinity and displayed the same tendency to form oligomers as the wild-type protein. We thus conclude that the role of Kar9 phosphorylation at the currently known sites is probably neither to regulate the stability of the Kar9-Bim1 complex nor to modulate the ability of Kar9 to form oligomers. However, we cannot exclude at this stage that the structure and the nature of the negatively charged side chain of a glutamic acid does not mimic a double negatively charged phosphoserine residue, as suggested previously (Moore and Miller, 2007). Furthermore, Ser-197, Ser-332, Ser-429, and Ser-496 are very likely not the only phosphorylated residues in Kar9; indeed, high-throughput studies have identified at least nine additional phosphorylation sites in vivo (Bodenmiller *et al.*, 2010; Swaney *et al.*, 2013). Therefore a more global analysis of Kar9 phosphorylation is now required to determine the role of phosphorylation in the context of Kar9's alternative tertiary interactions through allosteric changes and how Kar9 phosphorylation may cooperate with Bim1 phosphorylation in regulating complex formation.

Using different rationally designed Kar9 and Bim1 variants, we showed here that tight complex formation between Kar9 and Bim1 is mediated by the C-terminal domains of the two proteins. Previous pull-down experiments suggest that full-length Bim1 interacts with Kar9 from yeast extracts more efficiently than Bim1C, and a second Kar9-binding site has been mapped to the linker region of Bim1 between the CH and the C-terminal domain (Huls *et al.*, 2012). In our sedimentation velocity and ITC experiments, we observed that both Bim1 and Bim1C bind Kar9 with a similar nanomolar affinity, thus excluding additional high-affinity interaction sites between the two bacterially produced proteins. However, we also found that Site1 in Kar9 is fully functional only in the context of full-length Kar9. This result suggests that the context by which low- and high-affinity Bim1-binding sites are organized in Kar9, as well as their reciprocal collaboration, is important for the overall Bim1-binding capabilities of Kar9. However, we cannot exclude at this stage that, in yeast extracts, modified Kar9 may indeed present an additional binding site for the linker region besides the C-terminal domain of Bim1 (Huls *et al.*, 2012).

We found that bacterially produced Kar9 tightly interacts with Bim1 via three distinct sites present in the C-terminal disordered part of Kar9. Kar9 Site1 and Site2 are characterized by the presence
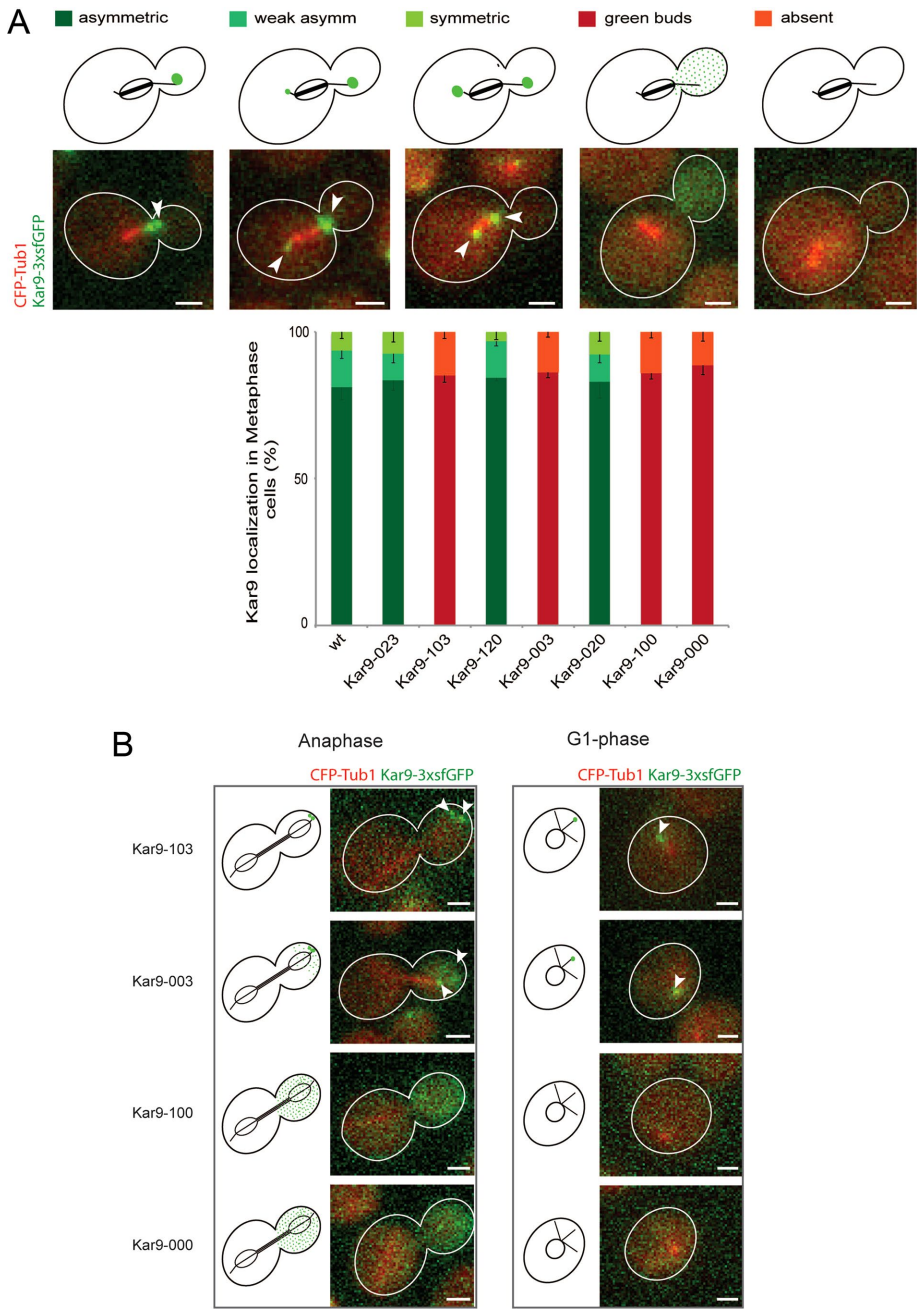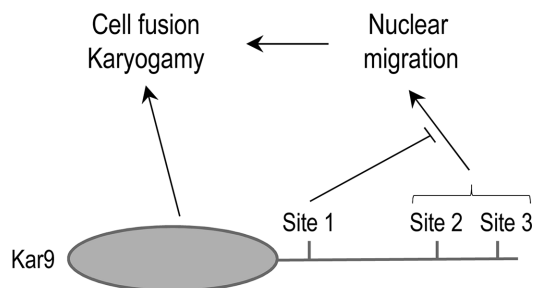
FIGURE 7: Site2 of Kar9 plays a preponderant role in Kar9 localization to the mitotic spindle. (A) Localization and quantification of the specified Kar9 alleles in metaphase cells. Same cells were quantified as in Figure 6, A and B; n > 186 cells per strain. White arrowheads point to the Kar9 foci. The mean ± SD of three independent clones was plotted. Scale bar: 1.5 μm. (B) Anaphase and G1-phase localization of Kar9-103, Kar9-003, Kar9-100, and Kar9-000. White arrowheads point to the Kar9 foci localized to the spindle. Scale bar: 1.5 μm.

Our reconstitution experiments of the microtubule-Mal3-Kar9 network indicate that the Kar9-Mal3 complex is not a dominant regulator of microtubule dynamics on its own in vitro. However, we note that these experiments were performed with a heterologous protein system (i.e., *S. pombe* Mal3 and *S. cerevisiae* Kar9 produced in bacteria, tubulin isolated from bovine brains) and therefore cannot exclude that the Kar9-Bim1 complex may have some effects on microtubule dynamics under more physiological conditions and/or when the proteins are posttranslationally modified. Our in vivo data in turn show that the Kar9-Bim1 interaction is functionally important throughout the cell cycle. They reveal that, during mating, Site2 and Site3 are equally important to ensure nuclear migration to the shmoo tip before cell fusion and karyogamy upon conjugation (Figure 8A). Remarkably, our study also establishes that Kar9 function in karyogamy is in part Bim1-independent and does not require Kar9 localization to microtubules. Indeed, the Kar9-000 variant, which does not bind Bim1 and is not visible on microtubules, is still able, to some extent, to promote karyogamy: the *kar9-000/kar9-000* mutant zygotes succeed much better in this process than the *kar9Δ* homozygous zygotes. Moreover, and surprisingly, our data reveal that, during metaphase, Site2 plays a key role in spindle positioning and alignment, while Site3 can no longer contribute to the Bim1-dependent function of Kar9 (Figure 8B). Site1, on the other hand, seems rather to play an inhibitory role during mating, while there is no evidence at this stage that it modulates Kar9 function during vegetative growth. These observations suggest that Site1 might contribute to regulating Kar9 function only when the Kar9-Bim1 complex is already preformed via Site2 and/or Site3; on its own, Site1 is not necessary to form the complex per se. This interpretation is consistent with Site1 showing some affinity to Bim1 only in the context of full-length Kar9.

Our observation that Site3 of Kar9 is potentially inactive during metaphase is consistent with the observation that less Bim1 is pulled down together with Kar9 when the latter is immunoprecipitated from extracts of metaphase yeast cells compared with extracts from G1-phase cells (Liakopoulos *et al.*, 2003). Nevertheless, concomitant mutation of Site2 and Site3 slightly increased the effects that the Site2 mutation alone had on the spindle, thus suggesting some functional role of Site3 for Kar9-Bim1 complex formation in vivo. The observation that both Site2 and Site3 are equally important during mating, but that Site2 is more important than Site3 during metaphase, is consistent with our in vitro results, wherein both sites contribute almost equally toward the high stability of the Kar9-Bim1 complex. The data also suggest

of SxIP-like and SxIP motifs, respectively, which are well known to act as microtubule-tip localization signals in many different +TIPs (Honnappa *et al.*, 2009; Buey *et al.*, 2012; Jiang *et al.*, 2012). In contrast, Site3 does not contain any recognizable EB1-binding motif; however, we pinpointed two residues, Pro-624 and Thr-625, which were crucial for Kar9 Site3 binding to Bim1. A detailed mutagenesis study in combination with a high-resolution complex structure is now needed to determine the exact amino acid requirements of Kar9 Site3 and its exact binding mode with the C-terminal domain of Bim1.

A Mating

Cell fusion
Karyogamy

Nuclear migration

Kar9

Site 1   Site 2   Site 3

B Metaphase

Spindle positioning/alignment

Kar9
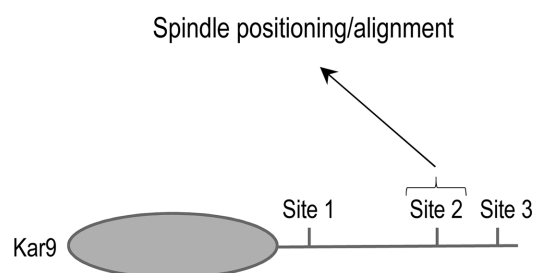
Site 1   Site 2   Site 3

FIGURE 8: Schematic representation of the role of the three Bim1-binding sites of Kar9 during mating and in metaphase. (A) During mating, Site2 and Site3 are equally important to ensure nuclear migration before cell fusion and karyogamy; the latter process is in part Bim1-independent and does not require Kar9 localization to microtubules. Site1 seems to play an inhibitory role during mating. (B) During metaphase, Site2 plays a key role in spindle positioning and alignment, while Site1 and Site3 do not seem to contribute to a Bim1-dependent function of Kar9 for vegetative growth. See the text for additional details. The N-terminal domain of Kar9 is indicated by the gray oval; the C-terminal part by a black line. The positions of Site1, Site2, and Site3 are indicated.

that Site3 could be subjected to posttranslational modifications in vivo. In this context, we noted that some of the residues previously found in high-throughput studies to be phosphorylated in vivo are located within or close to Site3 (Bodenmiller et al., 2010; Swaney et al., 2013). Notably, phosphorylation is a well-known mechanism to down-regulate the interaction of SxIP-motif containing +TIPs with EB1 family members (Honnappa et al., 2009; Kumar et al., 2009; Zimniak et al., 2012). As already elaborated, the importance and exact effects of posttranslational modifications on Kar9 function remains an important open question that necessitates further in-depth investigation.

The oligomerization properties of the N-terminal domain of Kar9 together with the three distinct Bim1-binding sites found in its C-terminal domain potentially enable Kar9 to recruit multiple Bim1 dimers to growing microtubule plus ends. Interestingly, another +TIP in which a moderately stable oligomerization domain is combined with multiple EB1-binding sites is SLAIN2. In mammalian cells, SLAIN2 acts as a phosphorylation-dependent scaffolding protein that interacts with and thus enables the microtubule polymerase ch-TOG (mammalian orthologue of *S. cerevisiae* Stu2) and the microtubule dynamics regulator CLIP-170 (mammalian orthologue of *S. cerevisiae* Bik1) to access growing microtubule tips in the crowded environment of the cell (Van der Vaart et al., 2011). Like SLAIN2, Kar9 binds Bim1/EB1, Stu2/ch-TOG, and Bik1/CLIP-170 (Moore

et al., 2006; Moore and Miller, 2007) and may thus represent a functional homologue of SLAIN2, at least with respect to its scaffolding properties. Notably, networks that are established by multivalent +TIPs could exhibit higher dwell times compared with the individual proteins alone, which might lead to a more stable association of +TIP assemblies with dynamic microtubule tips. Consistent with this hypothesis, fluorescence recovery after photobleaching of Kar9-GFP on astral microtubule plus ends is very slow, and a photoconvertible Kar9 variant remained associated with microtubules tips over the whole cell cycle after photoconversion (Liakopoulos et al., 2003; Kammerer et al., 2010). These observations suggest that Kar9 remains stably bound to astral microtubule plus ends and may thus represent a physical connector of microtubule tips to actin cables via the motor protein Myo2 (Yin et al., 2000; Hwang et al., 2003). Whether this behavior of Kar9 is linked to its high-affinity for Bim1 is an interesting avenue for further investigation.

In conclusion, our study shows for the first time that scaffolding proteins at microtubule tips, such as Kar9, can possess remarkably rich biochemical properties based on redundant but differentially tunable binding sites to adapt the function of the protein in the context of different cellular processes. Our results suggest that, depending on the need, the Kar9-Bim1 complex interacts with all cytoplasmic microtubules (during mating) or only with selected ones (during metaphase).

MATERIALS AND METHODS
Cloning and protein preparation
DNA sequences of all Kar9 and Bim1 constructs were PCR amplified from *S. cerevisiae* genomic DNA (S288C background). PCR products were subcloned into different bacterial expression vectors using the CloneEZ restriction-free method (GenScript, Piscataway, NJ) or homologous recombination in *Escherichia coli* cells (Olieric et al., 2010). Mutations were introduced by standard PCR-based site-directed mutagenesis techniques. The following expression vectors were used: Kar9 and Kar9-GFP, pACE (Bieniossek et al., 2009); Kar9N, NSKn1 (Olieric et al., 2010); Kar9C, PSTCm1 (Olieric et al., 2010); Trx-Kar9-site1 and Trx-Kar9-site2, PSPCm12 (Olieric et al., 2010); Bim1 and Bim1-GFP, pET3d (Invitrogen); and Bim1C and Bim1-GFP, PSTCm1.

Bim1 and Kar9 proteins were expressed in either the *E. coli* strain BL21(DE3; Invitrogen, Waltham, MA; Bim1 constructs) or Rosetta2 (DE3; Invitrogen; Kar9 constructs) in LB medium. Inoculated cultures were grown at 37°C until an OD_{600} of 0.6–0.8 was reached, induced with 0.7–1 mM isopropyl β-D-1-thiogalactopyranoside, and incubated overnight at 20°C. Cell pellets were resuspended in lysis buffer containing complete EDTA-free protease inhibitor mix (Roche Diagnostics, Basel, Switzerland) and a spatula tip of DNase I (Sigma-Aldrich, St. Louis, MO). Cells were lysed with a high-pressure homogenizer (Emulsiflex-C3 High Pressure Homogenize; Avestin, Ottawa, Canada). Cleared lysates were loaded onto HisTrap HP Ni^{2+}-Sepharose columns (GE Healthcare, Chicago, IL) at 4°C. After a washing step with buffers containing 50 mM imidazole, proteins were eluted with buffers containing 250 mM imidazole. The following buffers were used for Bim1 proteins: lysis/binding buffer, 500 mM NaCl, 20 mM Tris-HCl (pH 7.5), 5 mM imidazole, 2.5 mM β-mercaptoethanol; and elution buffer, 500 mM NaCl, 20 mM Tris-HCl (pH 7.5), 1 M imidazole, 2.5 mM β-mercaptoethanol. The following buffers were used for Kar9 proteins: lysis/binding buffer, 800 mM NaCl, 20 mM Tris-HCl (pH 7.5), 10% (vol/vol) glycerol, 5 mM imidazole, 2.5 mM β-mercaptoethanol; and elution buffer, 800 mM NaCl, 20 mM Tris-HCl (pH 7.5), 10% (vol/vol) glycerol, 1 M imidazole, 2.5 mM β-mercaptoethanol.

For all Bim1 proteins (with the exception of His-Bim1 used for the SPOT experiments) and Kar9-GFP, the 6xHis-tags of the proteins were removed by protease digestion with the respective protease while dialyzing against the lysis/binding buffer at the following conditions: Bim1 variants, overnight with TEV-protease at 4°C; Bim1C variants, overnight with human thrombin protease (Sigma-Aldrich) at room temperature; Kar9N, overnight with carboxypeptidase A from bovine pancreas (Sigma-Aldrich) at 4°C and in lysis/binding buffer without reducing agents; and Kar9-GFP, overnight with TEV-protease at 4°C. After cleavage, a second HisTrap column in lysis/binding buffer supplemented with 3% elution buffer was performed to separate cleaved from uncleaved protein.

After the Ni^{2+}-affinity purification step, Kar9C was subjected to cation-exchange chromatography. The protein eluted from the HisTrap column was diluted one- to sevenfold into 20 mM Bis-Tris-HCl (pH 6.0) and loaded onto a Resource 15S column (GE Healthcare). Kar9C was eluted and separated from degradation products by applying a gradient of 20–50% 20 mM Tris-HCl (pH 8.5), 1 M NaCl.

As a final purification step, all proteins were further purified by SEC on Superdex 75 or Superdex 200 columns (GE Healthcare) in the following buffers: Bim1 proteins, 150 mM NaCl, 20 mM Tris-HCl (pH 7.5), 10% (vol/vol) glycerol, 2.5 mM dithiothreitol (DTT); Bim1C proteins, 150 mM NaCl, 20 mM Tris-HCl (pH 7.5), 10% (vol/vol) glycerol; and Kar9 proteins, 800 mM NaCl, 20 mM Tris-HCl (pH 7.5), 10% (vol/vol) glycerol, 2.5 mM DTT. Pure protein fractions were concentrated by ultracentrifugation using Centriprep concentrators (Millipore, Billerica, MA), and aliquots were stored at −80°C.

Throughout all purification steps, the protein purity was assessed by Coomassie-stained SDS–PAGE. The identities of the protein samples were confirmed by electrospray ionization–time of flight mass spectrometry at the end of the purification. Mass spectrometry analysis of Kar9 and Bim1 yielded masses of 75.678 kDa and 38.287 kDa, respectively, which is in very good agreement with their theoretical masses (75.677 kDa for Kar9 and 38.2875 kDa for Bim1), thus demonstrating that our bacterially produced Kar9 and Bim1 protein samples are not posttranslationally modified. The purity of the protein preparations was typically > 95%. Protein quality after thawing was reassessed by SEC. Exact concentrations of protein solutions were determined by absorbance at 280 nm using a Nanodrop ND-1000 spectrometer (Thermo Fisher Scientific, Waltham, MA).

SEC-MALS

SEC-MALS experiments were performed at room temperature using a DAWN EOS 3-angle detector (Wyatt Technology Corporation, Santa Barbara, CA) followed by a Optilab Rex refractometer (Wyatt). Protein solutions (100 µl) were injected on a Superdex 200 10/300 GL (GE Healthcare) column equilibrated in the corresponding protein buffer. Molecular masses were calculated using the ASTRA V 5.3.4 software package (Wyatt). Bim1 and Bim1C were measured in 20 mM Tris-HCl (pH 7.5), 350 mM NaCl, 0.5 mM TCEP; and Kar9, Kar9N, and KarC were measured in 20 mM Tris-HCl (pH 7.5), 800 mM NaCl, 0.5 mM TCEP.

CD spectroscopy

Far-UV CD spectroscopy was performed using a Chirascan-plus spectrometer (Applied Photophysics, Surrey, United Kingdom) equipped with a temperature-controlled quartz cell (0.1 cm path length). Spectra were recorded at 4°C. A ramping rate of 1°C/min was used to record thermal unfolding profiles. Kar9 and Kar9N (4 µM each) were measured in 10 mM Na$_2$HPO$_4$/NaH$_2$PO$_4$ (pH 7.5), 800 mM NaCl; and Kar9C was measured in 10 mM Na$_2$HPO$_4$/NaH$_2$PO$_4$ (pH 7.5), 150 mM NaF.

AUC

All sedimentation velocity and equilibrium experiments were performed using an Optima XL-1 (Beckman Coulter, Brea, CA) AUC using either an An-50 Ti or An-60 Ti rotor (Beckman). Sedimentation velocity runs were recorded by measuring either absorbance at 280 or 230 nm or interference or fluorescence emission. A fluorescence-detection system (Aviv Biomedicals, Lakewood, NJ) was used to monitor the GFP fluorescence signal (λ_{ex} = 488 nm, λ_{em} = 505–565 nm). To avoid unspecific binding of protein to cell walls, we washed cells with buffer that was supplemented with 2 mg/ml bovine serum albumin (BSA) before loading protein samples.

Proteins for fluorescence-detection sedimentation velocity were in a buffer containing 20 mM Tris-HCl (pH 7.5), 350 mM NaCl, 10% (vol/vol) glycerol, 10 mM DTT, and 0.2 mg/ml BSA. All other measurements were performed in 80 mM PIPES-KOH (pH 6.8), 85 mM KCl, 4 mM MgCl$_2$, 1 mM ethylene glycol-bis(β-aminoethyl ether)-N,N,N',N'-tetraacetic acid (EGTA), 150 mM KOAc, 10 mM DTT, 0.2 mg/ml BSA.

Experiments were performed in charcoal-filled Epon double-sector velocity cells and sapphire glass windows. Data analysis was performed using the software package SEDFIT (Schuck, 2000). The partial specific volume was set to 0.73 ml/g for all measurements, and the solvent density and viscosity of the buffers used were calculated using SEDNTERP (http://bitcwiki.sr.unh.edu). All samples were measured at least in duplicate.

For the binding experiments, a mean and SD was calculated from at least two measurements per data point. Binding isotherms were obtained by fitting the data using the nonlinear curve-fitting tool in Origin 7 software (OriginLab, Northampton, MA) and the following equation, which describes the binding equilibrium as a function of the sedimentation coefficient, S, of fully free and fully bound species ($S_{Bim1(free)}$ and $S_{Bim1(bound)}$), the Kar9 and Bim1 concentration in the measured samples (Kar9$_{conc}$ and Bim1$_{conc}$), and the equilibrium dissociation constant, K_d, according to

$$S = S_{Bim1(free)} - (S_{Bim1(free)} - S_{Bim1(bound)}) * (Bim1_{conc} + Kar9_{conc} + K_d$$

$$- ((Bim1_{conc} + Kar9_{conc} + K_d)^2 - 4 * Bim1_{conc} * Kar9_{conc})^{0.5})$$

$$/ (2 * Bim1_{conc})$$

The K_d and $S_{Bim1(bound)}$ were fitted to the equation; $S_{Bim1(free)}$ was treated as a fixed constant.

Sedimentation equilibrium experiments were performed at 10°C in charcoal-filled Epon six sector cells at rotor speeds of 8000, 12,000, and 20,000 rpm. Proteins were in a buffer containing 20 mM Tris-HCl (pH 7.5), 350 mM NaCl, 10% (vol/vol) glycerol, 10 mM DTT, and 0.2 mg/ml BSA. Data analysis was performed using the Ultraspin software package (www.mrc-lmb.cam.ac.uk/dbv/ultraspin2).

ITC

ITC experiments were performed in 20 mM Na$_2$HPO$_4$/NaH$_2$PO$_4$ (pH 7.5), 150 mM NaCl at 25°C using an iTC200 (MicroCal Instruments, GE Lifesciences, Northampton MA) instrument. Ligand aliquots of 2.6 µl (250 µM) from the stirred syringe (1000 rpm) were injected 14 times into the sample cell containing protein (20 µM) with equilibration times of 150 s between injections. For determination of the binding stoichiometry and the equilibrium binding constant, isotherms were fitted using a nonlinear least squares minimization method provided with the ITC calorimeter (OriginLab, Northampton, MA) assuming the "one set of sites" binding model.

FCS

Before measurement, the thawed proteins used for FCS were resubjected to SEC using a Superdex 200 10/300 GL (GE Healthcare) column equilibrated in 20 mM Tris-HCl (pH 7.5), 800 mM NaCl, 10% (vol/vol) glycerol, 2 mM DTT to remove trace amounts of aggregated protein. Subsequently protein samples were diluted in 20 mM Tris-HCl (pH 7.5), 350 mM NaCl, 10% (vol/vol) glycerol, 10 mM DTT supplemented with 0.2 mg/ml BSA. All experiments were performed with 5 nM Bim1-GFP mixed with different amounts of Kar9. Samples (300 µl) were measured in four-chamber Nunc wells using a ZEISS LSM710 ConfoCor 3 microscope equipped with a Plan-Apochromat 40× water objective using an 488 argon laser (laser power 60 nW) and an Lp 505 filter. To avoid unspecific binding to the chamber walls, before samples were loaded, we incubated chambers with the above-indicated sample buffer supplemented with 2 mg/ml BSA. Experiments were performed at room temperature. All measurements for one binding isotherm were performed in the same chamber, starting with the sample with the lowest Kar9 concentration. Between measurements, the chamber was rinsed twice with 500 µl sample buffer. Data were analyzed using Ries, Bayer Opt Exp 2010 Software (Ries *et al.*, 2010). Each sample was measured 10 times for 1 min and a mean value and an SD was calculated from the corresponding diffusion times.

Binding isotherms were fitted to the data using the nonlinear curve fitting tool in Origin 7 software (OriginLab) and the following equation, which describes the binding equilibrium as a function of the diffusion time, τ, of fully free and fully bound species ($\tau_{Bim1(free)}$ and $\tau_{Bim1(bound)}$), the Kar9 and Bim1 concentration in the measured samples ($Kar9_{conc}$ and $Bim1_{conc}$), and the equilibrium dissociation constant, K_d, according to

$$\tau = \tau_{Bim1(free)} - (\tau_{Bim1(free)} - \tau_{Bim1(bound)}) * (Bim1_{conc} + Kar9_{conc} + K_d$$

$$- ((Bim1_{conc} + Kar9_{conc} + K_d)^2 - 4 * Bim1_{conc} * Kar9_{conc})^{0.5})$$

$$/ (2 * Bim1_{conc})$$

The K_d and $\tau_{Bim1(bound)}$ were fitted to the equation; $\tau_{Bim1(free)}$ was treated as a fixed constant.

SPOT

Cellulose membrane–bound peptide arrays were prepared according to standard SPOT synthesis protocols using a SPOT synthesizer as described in detail (Wenschuh *et al.*, 2000). The syntheses were performed on Whatman-50 cellulose membranes (Whatman, Maidstone, UK) using an automatic SPOT synthesizer (INTAVIS AG, Köln, Germany). The peptides were synthesized on amino-functionalized cellulose membranes of the ester type prepared by modifying a cellulose paper with Fmoc-β-alanine as the first spacer residue. In the second coupling step, the anchor position Fmoc-β-alanine-OPfp in dimethylsulfoxide was used. Residual amino functions between the spots were capped by acetylation. The Fmoc group was cleaved using 20% piperidine in dimethylformamide (DMF). The cellulose-bound peptide arrays were assembled on these membranes by using 0.3 M solutions of Fmoc-amino acid-OPfp in *N*-methyl-2-pyrrolidinone (NMP). Side-chain protection of the used Fmoc-amino acids was as follows: Glu, Asp (OtBu); Ser, Thr, Tyr (tBu); His, Lys, Trp (Boc); Asn, Gln, Cys (Trt); and Arg (Pbf). After the last coupling step, the acid-labile protection groups of the amino acid side chains were cleaved using 90% trifluoroacetic acid (TFA) for 30 min and 60% TFA for 3 h.

Membrane-bound Kar9 peptide variants were washed with DMF and ethanol and three times with TBS buffer (13.7 mM NaCl, 0.27 mM KCl, 5 mM Tris [Tris(hydroxymethyl)amino-methane, pH 8.0]) for 10 min each. Membranes were incubated for 3 h with blocking buffer (for 50 ml blocking buffer: 5 ml blocking buffer [Sigma-Aldrich, Steinheim, Germany], 2.5 g sucrose, 5 ml 10 × TBS buffer [137 mM NaCl, 2.7 mM KCl, 50 mM Tris, pH 8.0], filled up to 50 ml with water). Arrays were incubated with a solution of His-Bim1 at a concentration of 10 or 50 µg/ml in blocking buffer at room temperature overnight. After three washes with TBS buffer (10 min each), the arrays were incubated with a solution of a mouse antipolyhistidine immunoglobulin G (IgG) antibody (Sigma H-1029) in blocking buffer (dilution 1:10,000) for 3 h at room temperature and then washed three times with TBS. Afterward, the arrays were treated with a solution of a horseradish peroxidase–conjugated antimouse IgG antibody (Sigma A-5906) in blocking buffer (dilution 1:1000) at room temperature for 1.5 h; this was followed by three washes with TBS (10 min each). Binding was visualized by using a chemiluminescent substrate (Uptilight HRP, Uptima) and a Lumi-Imager (Roche Diagnostics).

We synthesized three replicas of the 15-mer and 24-mer peptide arrays. One set of the 15-mer/24-mer arrays were used as controls for detecting false positives; the other two sets were probed for His-Bim1 binding.

In vitro microtubule-tip tracking assay

In vitro reconstitution of microtubule end tracking using TIRF was performed as previously described (Bieling *et al.*, 2007; Gell *et al.*, 2010). In our hands, the assay did not produce robust and specific microtubule-tip localization of Bim1-GFP under the experimental conditions reported for this EB1 family member (Zimniak *et al.*, 2009), primarily due to the tendency of the bacterially produced protein to form aggregates on the cover slide. Bim1 and Mal3 contain 344 and 308 amino acid residues, respectively. Both proteins display the same domain organization, that is, a microtubule-binding CH domain that is followed by a predicted flexible linker and a partner-binding C-terminal domain encompassing the EB homology (EBH) domain. The CH and EBH domains share 67 and 54% sequence similarity, respectively. The linker region separating the CH and the EBH domain as well as the C-terminal tail regions is more divergent.

Briefly, guanosine-5′-[(a,b)-methyleno]triphosphate (GMPCPP)-stabilized microtubule seeds (15% Rhodamine labeled, 10% biotinylated) were adhered to base-washed and PEG-passivated coverslips via netravidin–steptavidin immobilization. Microtubule growth was initiated by the addition of 10 µM tubulin (2% Rhodamine labeled) and 1 mM GTP in assay buffer (80 mM PIPES-KOH, pH 6.8, 85 mM KCl, 4 mM MgCl, 1 mM EGTA, 150 mM KOAc) containing an oxygen scavenger system (0.02 mg/ml catalase, 1.5 mg/ml glucose oxidase, and 0.4 mg/ml glucose) and 0.1% methylcellulose. Protein concentrations were 100 nM for Mal3-GFP alone, and 100 nM Kar9-GFP together with 250 nM unlabeled Mal3. All experiments were carried out at 37°C.

Images were recorded on an Olympus IX81 inverted microscope equipped with a TIRF system and controlled by Olympus Cell⊥R software using an Olympus UAPON 100× TIRF objective (NA 1.49). Time-lapse images were acquired every 3 s over the duration of 6 min using a CCD camera (iXon[EM]+; Andor, Belfast, United Kingdom). Image analysis was performed using ImageJ, and kymographs were generated using the Kymograph plug-in written by Rietdorf and Seitz (www.embl.de/eamnet/html/body_kymograph .html). Microtubule dynamics parameters were determined as described previously (Blake-Hodek *et al.*, 2010).

Yeast (yYB) strain number	Mating type	Genotype
8597, 8600, 8602	a	CFP-Tub1:Trp1 kar9::His3 ura3-52 leu2 lys2-801 Ade2+
12656, 12657	a	CFP-Tub1:Trp1 kar9::Kar9-wt-3xsfGFP:KanMX ura3-52 his3Δ200 leu2 lys2-801 Ade2+
8461, 8462, 8463	a	CFP-Tub1:Trp1 kar9::Kar9-wt-3xGFP:KanMX ura3-52 his3Δ200 leu2 lys2-801 ade2-101
12640, 12641, 13166	a	CFP-Tub1:Trp1 kar9::Kar9-KKKNN-3xsfGFP:KanMX ura3-52 his3Δ200 leu2 lys2-801 Ade2+
9386, 9387,	a	CFP-Tub1:Trp1 kar9::Kar9-SRNN-3xGFP:KanMX ura3-52 his3Δ200 leu2 lys2-801 Ade2+
8468	a	CFP-Tub1:Trp1 kar9::Kar9-SRNN-3xGFP:KanMX ura3-52 his3Δ200 leu2 lys2-801 ade2-101
9388, 12654	a	CFP-Tub1:Trp1 kar9::Kar9-LxxAA-3xGFP:KanMX ura3-52 his3Δ200 leu2 lys2-801 Ade2+
8477	a	CFP-Tub1:Trp1 kar9::Kar9-LxxAA-3xGFP:KanMX ura3-52 his3Δ200 leu2 lys2-801 ade2-101
12642, 12643, 12644	a	CFP-Tub1:Trp1 kar9::Kar9-KKKNN SRNN-3xsfGFP:KanMX ura3-52 his3Δ200 leu2 lys2-801 Ade2+
12645, 12646, 12647	a	CFP-Tub1:Trp1 kar9::Kar9-KKKNN LxxAA-3xsfGFP:KanMX ura3-52 his3Δ200 leu2 lys2-801 Ade2+
8868, 9389	a	CFP-Tub1:Trp1 kar9::Kar9-SRNN LxxAA-3xGFP:KanMX ura3-52 his3Δ200 leu2 lys2-801 Ade2+
8472	a	CFP-Tub1:Trp1 kar9::Kar9-SRNN LxxAA-3xGFP:KanMX ura3-52 his3Δ200 leu2 lys2-801 ade2-101
12663, 12664, 12665	a	CFP-Tub1:Trp1 kar9::Kar9-KKKNN SRNN LxxAA-3xGFP:KanMX ura3-52 his3Δ200 leu2 lys2-801 Ade2+
6583	alpha	Nup82-3sfGFP::KanMX ura3 ade1 leu2
13383	alpha	CFP-Tub1:Trp1 kar9::His3 Cdc28-3xmKate:KanMX ura3-52 his3Δ200 leu2 lys2-801 Ade2+
13384	a	CFP-Tub1:Trp1 kar9::His3 Cdc28-3xmKate:KanMX ura3-52 his3Δ200 leu2 lys2-801 Ade2+
13465	alpha	CFP-Tub1:Trp1 kar9::His3 Nup82-3sfGFP:KanMX ura3-52 his3Δ200 leu2 lys2-801 Ade2+
13466	a	CFP-Tub1:Trp1 kar9::His3 Nup82-3sfGFP:KanMX ura3-52 his3Δ200 leu2 lys2-801 Ade2+
13389	alpha	CFP-Tub1:Trp1 kar9::Kar9-SRNN LxxAA-3xGFP:KanMX Cdc28-3xmKate:KanMX ura3-52 his3Δ200 leu2 lys2-801 Ade2+
13390	a	CFP-Tub1:Trp1 kar9::Kar9-SRNN LxxAA-3xGFP:KanMX Cdc28-3xmKate:KanMX ura3-52 his3Δ200 leu2 lys2-801 Ade2+
13467	alpha	CFP-Tub1:Trp1 kar9::Kar9-SRNN LxxAA-3xGFP:KanMX Nup82-3sfGFP:KanMX ura3-52 his3Δ200 leu2 lys2-801 Ade2+
13468	a	CFP-Tub1:Trp1 kar9::Kar9-SRNN LxxAA-3xGFP:KanMX Nup82-3sfGFP:KanMX ura3-52 his3Δ200 leu2 lys2-801 Ade2+
13395	a	CFP-Tub1:Trp1 kar9::Kar9-KKKNN LxxAA-3xGFP:KanMX Cdc28-3xmKate:KanMX ura3-52 his3Δ200 leu2 lys2-801 Ade2+
13396	alpha	CFP-Tub1:Trp1 kar9::Kar9-KKKNN LxxAA-3xGFP:KanMX Cdc28-3xmKate:KanMX ura3-52 his3Δ200 leu2 lys2-801 Ade2+
13425	a	CFP-Tub1:Trp1 kar9::Kar9-KKKNN LxxAA-3xGFP:KanMX Nup82-3sfGFP:KanMX ura3-52 his3Δ200 leu2 lys2-801 Ade2+
13426	alpha	CFP-Tub1:Trp1 kar9::Kar9-KKKNN LxxAA-3xGFP:KanMX Nup82-3sfGFP:KanMX ura3-52 his3Δ200 leu2 lys2-801 Ade2+
13393	alpha	CFP-Tub1:Trp1 kar9::Kar9-KKKNN SRNN-3xGFP:KanMX Cdc28-3xmKate:KanMX ura3-52 his3Δ200 leu2 lys2-801 Ade2+
13394	a	CFP-Tub1:Trp1 kar9::Kar9-KKKNN SRNN-3xGFP:KanMX Cdc28-3xmKate:KanMX ura3-52 his3Δ200 leu2 lys2-801 Ade2+
13423	a	CFP-Tub1:Trp1 kar9::Kar9-KKKNN SRNN-3xGFP:KanMX Nup82-3sfGFP:KanMX ura3-52 his3Δ200 leu2 lys2-801 Ade2+
13424	alpha	CFP-Tub1:Trp1 kar9::Kar9-KKKNN SRNN-3xGFP:KanMX Nup82-3sfGFP:KanMX ura3-52 his3Δ200 leu2 lys2-801 Ade2+

TABLE 4: Yeast strains used in this study.

Yeast (yYB) strain number	Mating type	Genotype
13397	alpha	CFP-Tub1:Trp1 kar9::Kar9-wt-3xsfGFP:KanMX Cdc28-3xmKate:KanMX ura3-52 his3Δ200 leu2 lys2-801 Ade2+
13398	a	CFP-Tub1:Trp1 kar9::Kar9-wt-3xsfGFP:KanMX Cdc28-3xmKate:KanMX ura3-52 his3Δ200 leu2 lys2-801 Ade2+
13469	alpha	CFP-Tub1:Trp1 kar9::Kar9-wt-3xGFP:KanMX Nup82-3sfGFP:KanMX ura3-52 his3Δ200 leu2 lys2-801 Ade2+
13470	a	CFP-Tub1:Trp1 kar9::Kar9-wt-3xGFP:KanMX Nup82-3sfGFP:KanMX ura3-52 his3Δ200 leu2 lys2-801 Ade2+
13399	a	CFP-Tub1:Trp1 kar9::Kar9-KKKNN-SRNN-LxxAA-3xsfGFP:KanMX Cdc28-3xmKate:KanMX ura3-52 his3Δ200 leu2 lys2-801 Ade2+
13400	alpha	CFP-Tub1:Trp1 kar9::Kar9-KKKNN-SRNN-LxxAA-3xsfGFP:KanMX Cdc28-3xmKate:KanMX ura3-52 his3Δ200 leu2 lys2-801 Ade2+
13427	alpha	CFP-Tub1:Trp1 kar9::Kar9-KKKNN-SRNN-LxxAA-3xsfGFP:KanMX Nup82-3sfGFP:KanMX ura3-52 his3Δ200 leu2 lys2-801 Ade2+
13428	alpha	CFP-Tub1:Trp1 kar9::Kar9-KKKNN-SRNN-LxxAA-3xsfGFP:KanMX Nup82-3sfGFP:KanMX ura3-52 his3Δ200 leu2 lys2-801 Ade2+

TABLE 4: Yeast strains used in this study. Continued

Yeast strains

All yeast strains used in this study are derived from the S288C background (Table 4). Kar9 proteins were tagged at the endogenous locus with 3xsfGFP:KanMX cassette. Specific Kar9 mutations were introduced on a pRS314-Kar9-3xsfGFP:KanMX centromeric plasmid via site-directed mutagenesis (Pfu Turbo; Stratagene, San Diego, CA). The Kar9 locus was then amplified and integrated in a *kar9Δ* strain, and the integration was confirmed by PCR and sequencing. CFP-Tub1 was inserted at the *TRP1* locus using the integrative plasmid pRS304. Cdc28 and Nup82 were endogenously tagged with the 3xmKate:kanMX and the 3xsfGFP:kanMX cassettes, respectively.

Growth conditions and fluorescence microscopy

G1 arrest. Exponentially grown cultures were diluted to $OD_{600} = 0.075$ in rich media, grown for 1.5 h at 25°C, and arrested with 6 mg/ml alpha-factor for 2 h. Nuclear positioning relative to the shmoo tip and Kar9 localization was assessed.

Mating. Exponentially grown isogenic cultures of opposite mating types were mixed at similar ODs, and cells were harvested by centrifugation at $600 \times g$ for 1 min and placed in imaging chambers under an agar pad lacking tryptophan. Cells were imaged every 10 min for a period of 2 h. Nuclear positioning and fusion were assessed at 40 min after the cytoplasmic fusion took place.

Vegetative growth. Yeast strains were exponentially grown in synthetic media lacking tryptophan. Cells were harvested by centrifugation at $600 \times g$ for 2 min and taken onto microscopy slides.

Strains were imaged on a Personal Delta Vision microscope, with z-stacks of 11 layers (step size of 0.3 μm). Images were analyzed with Fiji (ImageJ) using sum projections.

REFERENCES

Bieling P, Laan L, Schek H, Munteanu EL, Sandblad L, Dogterom M, Brunner D, Surrey T (2007). Reconstitution of a microtubule plus-end tracking system in vitro. Nature 450, 1100–1105.

Bieniossek C, Nie Y, Frey D, Olieric N, Schaffitzel C, Collinson I, Romier C, Berger P, Richmond TJ, Steinmetz MO, *et al.* (2009). Automated unrestricted multigene recombineering for multiprotein complex production. Nat Methods 6, 447–450.

Blake-Hodek KA, Cassimeris L, Huffaker TC (2010). Regulation of microtubule dynamics by Bim1 and Bik1, the budding yeast members of the EB1 and CLIP-170 families of plus-end tracking proteins. Mol Biol Cell 21, 2013–2023.

Bodenmiller B, Wanka S, Kraft C, Urban J, Campbell D, Pedrioli PG, Gerrits B, Picotti P, Lam H, Vitek O, *et al.* (2010). Phosphoproteomic analysis reveals interconnected system-wide responses to perturbations of kinases and phosphatases in yeast. Sci Signal 3, rs4.

Buey RM, Sen I, Kortt O, Mohan R, Gfeller D, Veprintsev D, Kretzschmar I, Scheuermann J, Neri D, Zoete V, *et al.* (2012). Sequence determinants of a microtubule tip localization signal (MtLS). J Biol Chem 287, 28227–28242.

Conde J, Fink GR (1976). A mutant of *Saccharomyces cerevisiae* defective for nuclear fusion. Proc Natl Acad Sci USA 73, 3651–3655.

Frank R (2002). The SPOT-synthesis technique. Synthetic peptide arrays on membrane supports—principles and applications. J Immunol Methods 267, 13–26.

Gell C, Bormuth V, Brouhard GJ, Cohen DN, Diez S, Friel CT, Helenius J, Nitzsche B, Petzold H, Ribbe J, *et al.* (2010). Microtubule dynamics reconstituted in vitro and imaged by single-molecule fluorescence microscopy. Methods Cell Biol 95, 221–245.

Hartwell LH (1973). Synchronization of haploid yeast cell cycles, a prelude to conjugation. Exp Cell Res 76, 111–117.

Heil-Chapdelaine RA, Oberle JR, Cooper JA (2000). The cortical protein Num1p is essential for dynein-dependent interactions of microtubules with the cortex. J Cell Biol 151, 1337–1344.

Herskowitz I (1988). Life cycle of the budding yeast *Saccharomyces cerevisiae*. Microbiol Rev 52, 536–553.

Honnappa S, Gouveia SM, Weisbrich A, Damberger FF, Bhavesh NS, Jawhari H, Grigoriev I, van Rijssel FJ, Buey RM, Lawera A, *et al.* (2009). An EB1-binding motif acts as a microtubule tip localization signal. Cell 138, 366–376.

Hotz M, Leisner C, Chen D, Manatschal C, Wegleiter T, Ouellet J, Lindstrom D, Gottschling DE, Vogel J, Barral Y (2012). Spindle pole bodies exploit the mitotic exit network in metaphase to drive their age-dependent segregation. Cell 148, 958–972.

Huls D, Storchova Z, Niessing D (2012). Post-translational modifications regulate assembly of early spindle orientation complex in yeast. J Biol Chem 287, 16238–16245.

Hwang E, Kusch J, Barral Y, Huffaker TC (2003). Spindle orientation in *Saccharomyces cerevisiae* depends on the transport of microtubule ends along polarized actin cables. J Cell Biol 161, 483–488.

Jiang K, Toedt G, Montenegro Gouveia S, Davey NE, Hua S, van der Vaart B, Grigoriev I, Larsen J, Pedersen LB, Bezstarosti K, *et al.* (2012). A proteome-wide screen for mammalian SxIP motif-containing microtubule plus end tracking proteins. Curr Biol 22, 1800–1807.

Kammerer D, Stevermann L, Liakopoulos D (2010). Ubiquitylation regulates interactions of astral microtubules with the cleavage apparatus. Curr Biol 20, 1233–1243.

Katsuki M, Drummond DR, Osei M, Cross RA (2009). Mal3 masks catastrophe events in *Schizosaccharomyces pombe* microtubules by inhibiting shrinkage and promoting rescue. J Biol Chem 284, 29246–29250.

Korinek WS, Copeland MJ, Chaudhuri A, Chant J (2000). Molecular linkage underlying microtubule orientation toward cortical sites in yeast. Science 287, 2257–2259.

Kumar P, Lyle KS, Gierke S, Matov A, Danuser G, Wittmann T (2009). GSK-3beta phosphorylation modulates CLASP-microtubule association and lamella microtubule attachment. J Cell Biol 184, 895–908.

Kurihara LJ, Beh CT, Latterich M, Schekman R, Rose MD (1994). Nuclear congression and membrane fusion: two distinct events in the yeast karyogamy pathway. J Cell Biol 126, 911–923.

Kusch J, Liakopoulos D, Barral Y (2003). Spindle asymmetry: a compass for the cell. Trends Cell Biol 13, 562–569.

Kusch J, Meyer A, Snyder MP, Barral Y (2002). Microtubule capture by the cleavage apparatus is required for proper spindle positioning in yeast. Genes Dev 16, 1627–1639.

Lee L, Tirnauer JS, Li J, Schuyler SC, Liu JY, Pellman D (2000). Positioning of the mitotic spindle by a cortical-microtubule capture mechanism. Science 287, 2260–2262.

Leisner C, Kammerer D, Denoth A, Britschi M, Barral Y, Liakopoulos D (2008). Regulation of mitotic spindle asymmetry by SUMO and the spindle-assembly checkpoint in yeast. Curr Biol 18, 1249–1255.

Liakopoulos D, Kusch J, Grava S, Vogel J, Barral Y (2003). Asymmetric loading of Kar9 onto spindle poles and microtubules ensures proper spindle alignment. Cell 112, 561–574.

Maddox P, Chin E, Mallavarapu A, Yeh E, Salmon ED, Bloom K (1999). Microtubule dynamics from mating through the first zygotic division in the budding yeast *Saccharomyces cerevisiae*. J Cell Biol 144, 977–987.

Maekawa H, Schiebel E (2004). Cdk1-Clb4 controls the interaction of astral microtubule plus ends with subdomains of the daughter cell cortex. Genes Dev 18, 1709–1724.

Maekawa H, Usui T, Knop M, Schiebel E (2003). Yeast Cdk1 translocates to the plus end of cytoplasmic microtubules to regulate bud cortex interactions. EMBO J 22, 438–449.

Miller RK, Cheng SC, Rose MD (2000). Bim1p/Yeb1p mediates the Kar9p-dependent cortical attachment of cytoplasmic microtubules. Mol Biol Cell 11, 2949–2959.

Miller RK, Rose MD (1998). Kar9p is a novel cortical protein required for cytoplasmic microtubule orientation in yeast. J Cell Biol 140, 377–390.

Molk JN, Salmon ED, Bloom K (2006). Nuclear congression is driven by cytoplasmic microtubule plus end interactions in *S. cerevisiae*. J Cell Biol 172, 27–39.

Montenegro Gouveia S *et al.* (2010). In vitro reconstitution of the functional interplay between MCAK and EB3 at microtubule plus ends. Curr Biol 20, 1717–1722.

Moore JK, D'Silva S, Miller RK (2006). The CLIP-170 homologue Bik1p promotes the phosphorylation and asymmetric localization of Kar9p. Mol Biol Cell 17, 178–191.

Moore JK, Miller RK (2007). The cyclin-dependent kinase Cdc28p regulates multiple aspects of Kar9p function in yeast. Mol Biol Cell 18, 1187–1202.

Olieric N, Kuchen M, Wagen S, Sauter M, Crone S, Edmondson S, Frey D, Ostermeier C, Steinmetz MO, Jaussi R (2010). Automated seamless DNA co-transformation cloning with direct expression vectors applying positive or negative insert selection. BMC Biotechnol 10, 56.

Ries J, Bayer M, Csucs G, Dirkx R, Solimena M, Ewers H, Schwille P (2010). Automated suppression of sample-related artifacts in fluorescence correlation spectroscopy. Opt Express 18, 11073–11082.

Schuck P (2000). Size-distribution analysis of macromolecules by sedimentation velocity ultracentrifugation and Lamm equation modeling. Biophys J 78, 1606–1619.

Sen I, Veprintsev D, Akhmanova A, Steinmetz MO (2013). End binding proteins are obligatory dimers. PLoS One 8, e74448.

Sheltzer JM, Rose MD (2009). The class V myosin Myo2p is required for Fus2p transport and actin polarization during the yeast mating response. Mol Biol Cell 20, 2909–2919.

Slep KC (2010). Structural and mechanistic insights into microtubule end-binding proteins. Curr Opin Cell Biol 22, 88–95.

Swaney DL, Beltrao P, Starita L, Guo A, Rush J, Fields S, Krogan NJ, Villen J (2013). Global analysis of phosphorylation and ubiquitylation cross-talk in protein degradation. Nat Methods 10, 676–682.

van der Vaart B, Manatschal C, Grigoriev I, Olieric V, Gouveia SM, Bjelic S, Demmers J, Vorobjev I, Hoogenraad CC, Steinmetz MO, *et al.* (2011). SLAIN2 links microtubule plus end-tracking proteins and controls microtubule growth in interphase. J Cell Biol 193, 1083–1099.

Volkmer R (2009). Synthesis and application of peptide arrays: quo vadis SPOT technology. Chembiochem 10, 1431–1442.

Wenschuh H, Volkmer-Engert R, Schmidt M, Schulz M, Schneider-Mergener J, Reineke U (2000). Coherent membrane supports for parallel microsynthesis and screening of bioactive peptides. Biopolymers 55, 188–206.

Yin H, Pruyne D, Huffaker TC, Bretscher A (2000). Myosin V orientates the mitotic spindle in yeast. Nature 406, 1013–1015.

Zimniak T, Fitz V, Zhou H, Lampert F, Opravil S, Mechtler K, Stolt-Bergner P, Westermann S (2012). Spatiotemporal regulation of Ipl1/Aurora activity by direct Cdk1 phosphorylation. Curr Biol 22, 787–793.

Zimniak T, Stengl K, Mechtler K, Westermann S (2009). Phosphoregulation of the budding yeast EB1 homologue Bim1p by Aurora/Ipl1p. J Cell Biol 186, 379–391.